The Astrophysical Journal, 951:101 (18pp), 2023 July 10 https://doi.org/10.3847/1538-4357/accd5d

Mapping the Skies of Ultracool Worlds: Detecting Storms and Spots with Extremely Large Telescopes

Michael K. Plummer and Ji Wang (王吉)
Department of Astronomy, The Ohio State University, 140 W. 18th Avenue, Columbus, OH 43210, USA; plummer.323@buckeyemail.osu.edu
Received 2023 February 1; revised 2023 April 4; accepted 2023 April 14; published 2023 July 6

Abstract

Extremely large telescopes (ELTs) present an unparalleled opportunity to study the magnetism, atmospheric dynamics, and chemistry of very-low-mass (VLM) stars, brown dwarfs, and exoplanets. Instruments such as the Giant Magellan Telescope–Consortium Large Earth Finder (GMT/GCLEF), the Thirty Meter Telescope's Multi-Objective Diffraction-limited High-Resolution Infrared Spectrograph (TMT/MODHIS), and the European Southern Observatory's Mid-Infrared ELT Imager and Spectrograph (ELT/METIS) provide the spectral resolution and signal-to-noise ratio necessary to Doppler image ultracool targets' surfaces based on temporal spectral variations due to surface inhomogeneities. Using our publicly available code, `Imber`, developed and validated in Plummer & Wang, we evaluate these instruments' abilities to discern magnetic starspots and cloud systems on a VLM star (TRAPPIST-1), two L/T transition ultracool dwarfs (VHS J1256−1257 b and SIMP J0136+0933), and three exoplanets (Beta Pic b and HR 8799 d and e). We find that TMT/MODHIS and ELT/METIS are suitable for Doppler imaging the ultracool dwarfs and Beta Pic b over a single rotation. Uncertainties for longitude and radius are typically $\lesssim$10°, and latitude uncertainties range from ∼10° to 30°. TRAPPIST-1's edge-on inclination and low $v \sin i$ provide a challenge for all three instruments, while GMT/GCLEF and the HR 8799 planets may require observations over multiple rotations. We compare the spectroscopic technique, photometry-only inference, and the combination of the two. We find combining spectroscopic and photometric observations can lead to improved Bayesian inference of surface inhomogeneities and offers insight into whether ultracool atmospheres are dominated by spotted or banded features.

Unified Astronomy Thesaurus concepts: Exoplanet atmospheres (487); Brown dwarfs (185); Late-type dwarf stars (906); Doppler imaging (400); Direct imaging (387)

1. Introduction

Over the next decade, first-light instruments are planned to come on-line for extremely large telescopes (ELTs), including the Giant Magellan Telescope–Consortium Large Earth Finder (GMT/GCLEF; Szentgyorgyi et al. 2018), the Thirty Meter Telescope's Multi-Objective Diffraction-limited High-Resolution Infrared Spectrograph (TMT/MODHIS; Mawet et al. 2019), and the European Southern Observatory's (ESO) Mid-Infrared ELT Imager and Spectrograph (ELT/METIS; Brandl et al. 2021). Spectra collected with these instruments will have the requisite spectral resolution and signal-to-noise ratio (S/N) to map temperature variations and chemical inhomogeneities created by magnetic spots and clouds in ultracool atmospheres.

Ultracool objects include very-low-mass (VLM) stars, brown dwarfs (BDs), and directly imaged extrasolar giant planets (EGPs). With effective temperatures $\lesssim$2700 K, these ultracool atmospheres allow the formation of metal and silicate condensates (Tsuji et al. 1996a; Jones & Tsuji 1997; Allard et al. 2001; Helling et al. 2008; Witte et al. 2011). The hottest ultracool objects, such as late M dwarfs and early L dwarfs, may contain both magnetic starspots and mineral clouds, driving optical and near-infrared (NIR) variability (Lane et al. 2007; Heinze et al. 2013; Gizis et al. 2015; Dulaimi et al. 2023). Cooler BDs and EGPs likely experience variability driven by cloud systems and planetary banding (Reiners & Basri 2008; Apai et al. 2013, 2017, 2021; Zhou et al. 2022).

Magnetic starspots and associated stellar activity can influence the atmospheres and habitability of planets with VLM stellar hosts. Although M dwarfs are more likely to host terrestrial planets than solar-type stars (Mulders et al. 2015; Tuomi et al. 2019; Zink et al. 2020; Sabotta et al. 2021), late-type stars possess enhanced stellar activity and close-in habitable zones, which could promote atmospheric escape and hinder the development of life (Kasting et al. 1993; Scalo et al. 2007; Zendejas et al. 2010; Kopparapu et al. 2013; Günther et al. 2020). The orientation of high-energy events could affect the radiation experienced by short-period planets. Doppler imaging (Barnes et al. 2015, 2017) and TESS photometry (Ilin et al. 2021; Martin et al. 2023) tentatively suggest a bias toward high-latitude starspot formation and flare eruption in M dwarfs, respectively. Follow-on observations and a statistical study can be accomplished by future ELT instruments.

The condensation and subsequent precipitation of atmospheric mineral clouds has been proposed to explain both the reddening of L-dwarf spectra as BDs cool across their lifetimes and the transition starting at ∼1300 K to relatively cloud-free and blue mid-to-late T-dwarf spectra (Tsuji et al. 1996b; Ackerman & Marley 2001; Allard et al. 2001; Saumon & Marley 2008). This L/T transition is associated with both the emergence of methane absorption (Oppenheimer et al. 1995; Noll et al. 2000) and an increase in spectral and photometric variability (Radigan et al. 2014; Radigan 2014; Eriksson et al. 2019), potentially due to patchy clouds (Ackerman &

Table 1
Instrument Comparison Summary

Instrument	Mode	λ_{range} (μm)	R	Δv_{avg} (km s^{-1})	Throughput	Area (m^2)	Sources
GMT/GCLEF	PRV[a]	0.35–0.95[a]	105,000[a]	2.86	0.11[a]	368[b]	[a]Szentgyorgyi et al. (2018) [b]Johns (2006)
TMT/MODHIS	N/A	0.95–2.4[a]	100,000[a]	3.00	0.1[b]	664.2[c]	[a]Mawet et al. (2019) [b]www.tmt.org/page/modhis [c]Skidmore et al. (2015)
ELT/METIS	IFU[a]	3.65–3.95[a]	100,000[a]	3.00	0.25[b]	978[c]	[a]Brandl et al. (2021) [b]www.eso.org/observing/etc/ [c]https://elt.eso.org/about/facts/
	L-band Imaging[a]	3.475–4.105[a]	N/A	N/A	0.5[b]		

Marley 2001; Marley et al. 2002, 2010) or layers with varying temperatures and opacities (Radigan et al. 2012; Apai et al. 2013; Buenzli et al. 2014). A Doppler imaging map of Luhman 16B, an early T dwarf, supports these patchy and layered models (Crossfield et al. 2014).

Due to their similar temperature and spectral characteristics, field BDs have often been treated as high-surface-gravity analogs and used as stepping stones for EGPs. Studies of exoplanet-analog, planetary-mass objects (PMOs) such as 2MASS J2139+02 (Apai et al. 2013; Yang et al. 2016; Vos et al. 2023), PSO J318.5−22 (Biller et al. 2015, 2018), 2MASS 1207 b (Zhou et al. 2016), VHS J1256−1257 b (henceforth VHS 1256 b; Zhou et al. 2020b; Bowler et al. 2020; Zhou et al. 2022), and SIMP J0136+0933 (henceforth SIMP 0136; Artigau et al. 2009; Apai et al. 2013; Yang et al. 2016; Vos et al. 2023) have demonstrated variability to be common for these objects. However, upcoming telescopes will directly address EGPs' spectral and photometric variations with comparable S/N.

Similar to BDs, EGPs demonstrate increasingly red spectra with evidence of extensive cloud coverage across the L class, but for planets such as HR 8799 bcde this track appears to continue to temperatures below ∼1300 K (Allers & Liu 2013; Bonnefoy et al. 2014; Zurlo et al. 2016; Zhang 2020). Cooler EGPs, such as 51 Eri b (Macintosh et al. 2015) and GJ 504 b (Liu et al. 2016), manifest the color and J-band absolute magnitude commensurate with T dwarfs, perhaps indicating that the L/T transition occurs later for low-gravity planetary objects (Biller et al. 2018).

Previously, in Plummer & Wang (2022), we developed a unified spectroscopic and photometric analytical technique to infer surface inhomogeneities such as magnetic starspots, cloud systems, and atmospheric vortices in ultracool objects. In this paper, we use that technique to estimate the ability of ELTs to detect spots and storms in ultracool targets. We also introduce our publicly available Python code, `Imber`,[1] which uses the methods detailed in Plummer & Wang (2022) to both numerically simulate spectroscopic and photometric surface inhomogeneities and to analytically infer such features on astrophysical targets.

In Section 2, we describe GMT/GCLEF, TMT/MODHIS, and ELT/METIS and demonstrate `Imber`'s internal S/N calculator. In Section 3, we describe our methods, including how we produce simulated observations for each target, a review of our analytical technique, and how the method is used to generate and fit time-resolved spectroscopic and photometric observations. We then apply our method to six targets (TRAPPIST-1, VHS 1256 b, SIMP 0136, Beta Pic b, and HR 8799 d and e) in Section 4 to determine the feasibility of Doppler imaging with each instrument. We explore combining spectroscopy and photometry to improve retrievals in Section 5, and summarize our results in Section 6.

2. Instruments

We will provide an overview of each telescopes' attributes and the instruments' scientific capabilities. We will then outline our process for adapting the S/N calculator originally created for the ESO ELT spectroscopic Exposure Time Calculator (ETC) into a submodule within `Imber`. To demonstrate our S/N computations' validity, we compare `Imber`'s outputs to those obtained from the ELT spectroscopic ETC. The instrument and telescope parameters are summarized in Table 1.

To limit the scope of this work, we focus on first-light, high-spectral-resolution instruments. The GMT/Near-Infrared (IR) Spectrograph (Jaffe et al. 2016) offers reasonably high spectral resolution ($R \sim 65{,}000$ (JHK), 85,000 (LM)) and ideal wavelength coverage ($1.1 < \lambda < 5.4\ \mu$m), but as the instrument requires adaptive optics (AO) unavailable at first light, we do not include it. Planned (and conceptual) second-generation, high-spectral-resolution instruments such as the TMT's Planet System Imager (Fitzgerald et al. 2019), Mid-IR Camera, High-Disperser and IFU Spectrograph (Packham et al. 2014), High-Resolution Optical Spectrometer (Froning et al. 2006), and the ELT's Armazones High Dispersion Echelle Spectrograph (Marconi et al. 2022) are also left to future works. Our publicly available and open-source Python code, `Imber`, will conveniently allow second-generation and beyond instrument performance to be evaluated using the methodology outlined in this paper.

2.1. Giant Magellan Telescope–Consortium Large Earth Finder

The GMT is an integral component of the United States' ELT Program (US-ELTP) with a first light expected in the mid-2030s (Fanson et al. 2020; National Academies of Sciences, Engineering, & Medicine 2021). Its primary mirror consists of seven 8.4 m diameter segments with a deformable secondary mirror comprised of seven, conjugate-paired 1.05 m diameter mirrors (Johns 2006). GMT provides the infrared (IR) diffraction-limited performance of a 24.5 m aperture and a collecting area (368 m^2) equivalent to a 21.9 m telescope (Johns 2006). Notably, unlike the two larger ELTs, AO/high-

[1] https://github.com/mkplummer/Imber

contrast imaging (HCI) are not scheduled to be implemented at GMT's first light (McCarthy et al. 2016; Mawet et al. 2019; Brandl et al. 2021).

GMT/GCLEF is a visible-light Echelle spectrograph and first-light instrument for the telescope (Szentgyorgyi et al. 2018). Operating in its precision radial velocity (PRV) mode, GMT/GCLEF has a top spectral resolution of 105,000 (corresponding to an average velocity per resolution element of $\Delta v_{\rm avg} = 2.86\,{\rm km\,s^{-1}}$). The instrument has a peak throughput of 11% and possesses both blue (350–540 nm) and red (540–900 nm) spectral channels (Szentgyorgyi et al. 2018). Due to the relatively cool effective temperatures of the targets considered in this paper, we will only be using the GMT/GCLEF red channel for our analysis.

GMT will be built at the Las Campanas Observatory (LCO; Thomas-Osip et al. 2008). Due to lack of publicly available sky emission and transmission models for the GMT site, for this paper we will approximate the LCO sky model with ESO's SkyCalc tool evaluated using the Cerro Paranal Advanced Sky Model (Noll et al. 2012; Jones et al. 2013). We assume an airmass of 1.5, precipitable water vapor (PWV) of 2.5 mm, and include scattered starlight, zodiacal light, upper and lower atmospheric emission, and airglow in the radiance model.

2.2. Thirty Meter Telescope Multi-Objective Diffraction-limited High-Resolution Infrared Spectrograph

The TMT is also part of the US-ELTP, and, similar to GMT, has an expected first light in the mid-2030s (National Academies of Sciences, Engineering, & Medicine 2021). TMT will be the only ELT located in the Northern Hemisphere (National Academies of Sciences, Engineering, & Medicine 2021). The TMT has a diameter of 30 m with a total collecting area of 664.2 m^2 (Skidmore et al. 2015). The telescope is capable of observing in wavelengths ranging from 0.31 to 28 μm (Skidmore et al. 2015).

TMT/MODHIS is a diffraction-limited, high-resolution spectrograph ($R \sim 100{,}000$, $\Delta v_{\rm avg} = 3.00\,{\rm km\,s^{-1}}$; Mawet et al. 2019). With simultaneous NIR wavelength coverage ranging from 0.95 to 2.4 μm (Mawet et al. 2019), the instrument has an estimated throughput of ~10%.[2]

The building site for TMT has yet to be determined, but the two final contenders are Maunakea, Hawaii and the Observatorio del Roque de Los Muchachos (ORM) in La Palma, Canary Islands, Spain.[3] For the purposes of this paper, we will utilize the publicly available sky emission and transmission tables for Maunakea (Lord 1992; Maihara et al. 1993), but our code will allow a simple change to accommodate the potential ORM site. These models use an atmospheric temperature of 273 K, and we assume an airmass of 1.5 and PWV of 1.0 mm for both the emission and transmission models.

2.3. European Southern Observatory Mid-Infrared ELT Imager and Spectrograph

The European ELT (E-ELT), designed and operated by ESO, expects first light in 2028.[4] E-ELT will have a diameter of 39 m and is comprised of 798 segments.[5] With a 978 m^2 collecting area, at the time of its completion it will be the largest optical and IR telescope in the world.[6]

ELT/METIS is capable of high-resolution spectroscopy ($R \sim 100{,}000$, $\Delta v_{\rm avg} = 3.00\,{\rm km\,s^{-1}}$) and HCI with coronagraphy in the NIR and mid-IR regions (3 to 13 μm; Brandl et al. 2021). For Doppler imaging, we are interested in its integral field unit (IFU) spectroscopy modes in the *L* and *M* bands, which can also be combined with coronagraphy. We will use the extended-wavelength option, which covers 300 nm (Brandl et al. 2021), to increase the effectiveness of spectral deconvolution (discussed with more detail in Section 3).

ELT/METIS also contains an imager with both continuum and spectral-feature modes (Brandl et al. 2021). Notably, ELT/METIS is capable of switching between spectroscopic and imaging modes within seconds, allowing for near-simultaneous, multimodal observations (B. Brandl, private communication).

E-ELT will be built at Cerro Armazones in Chile's Atacama Desert. For our sky emission and transmission models, we again use the ESO SkyCalc Tool (Noll et al. 2012; Jones et al. 2013) and select the high-altitude location to best approximate Cerro Armazones. We make the same airmass, PWV, and radiance model assumptions as described for GMT/GCLEF.

2.4. Instrument Signal-to-noise Ratio Computation

Computing the three instruments' S/Ns for each target described in Section 4 is key to generating accurate simulated spectra, line profiles (LPs), and light curves. In this paper, we adopt the methodology used in the ESO ELT spectroscopic and imaging ETCs, which use the following formula (modified here to account for host starlight suppression):[7]

$$\mathrm{S/N} = \frac{\sqrt{n_{\rm exp}}N_{\rm obj}}{\sqrt{N_{\rm obj} + CN_{\rm host} + N_{\rm sky} + N_{\rm pix}r^2 + N_{\rm pix}dT}}, \quad (1)$$

where $n_{\rm exp}$ is the number of exposures and $N_{\rm obj}$ is the number of electrons measured from the target. For targets requiring HCI, C is the starlight suppression level and $N_{\rm host}$ is the number of electrons from the host star. $N_{\rm sky}$ is the number of electrons detected from the background sky, $N_{\rm pix}$ is the number of detector pixels for which the observed light is distributed, r is readout noise, d is detector dark current, and T is exposure time. The exposure time and quantity is set by the observer while readout noise and dark current depend on the detector used in the instrument. $N_{\rm pix}$ is also instrument dependent, while $N_{\rm sky}$ is computed using the sky emission and transmission tables in tandem with the instrument's S/N reference area, the angular extent of the sky for which photons are collected.[8]

Calculating $N_{\rm obj}$ requires the target's apparent magnitude and template (synthetic) spectrum as well as the observing instrument's wavelength band, collecting area, throughput/efficiency, and effective diameter. The apparent magnitude determines how much flux from the target is available in a particular photometric band. The template spectrum is then scaled to the photometric flux to produce the mocked observation flux. This flux, along with the collecting area, throughput, and efficiency determine the number of photons

[2] www.tmt.org/page/modhis
[3] www.tmt.org/page/site
[4] https://elt.eso.org/about/timeline/
[5] https://elt.eso.org/mirror
[6] www.eso.org/public/archives/annualreports/pdf/ar_2021.pdf
[7] www.eso.org/observing/etc/
[8] www.eso.org/observing/etc/doc/elt/etc_spec_model.pdf

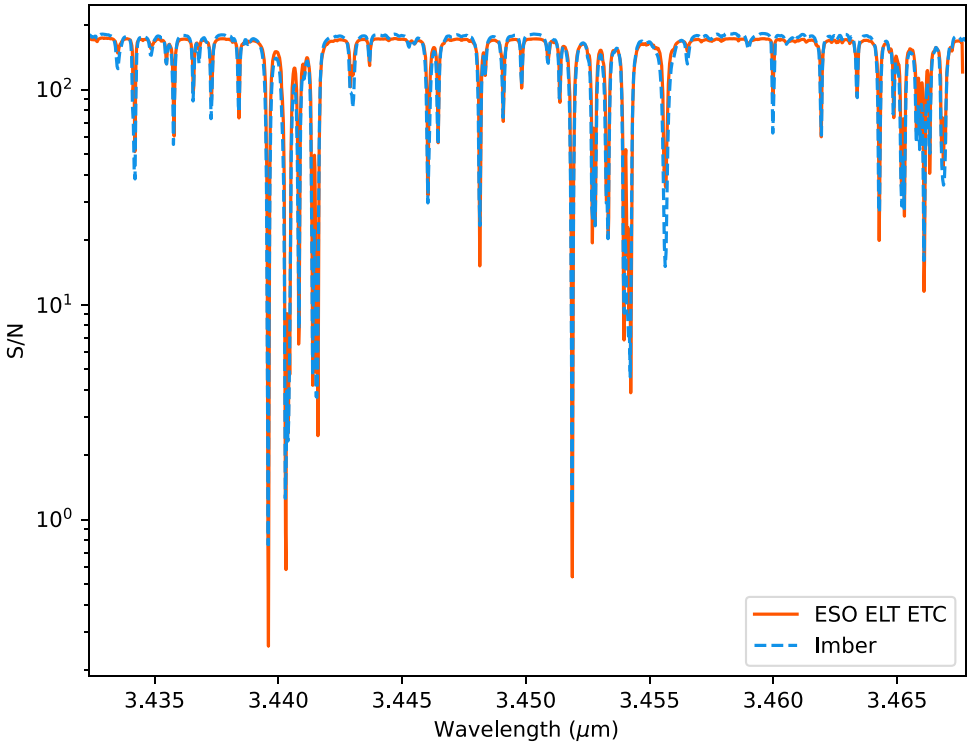

Figure 1. Spectral S/N comparison between ESO's ELT spectroscopic ETC and `Imber` using the same methodology. For comparison, a 1500 K object with an apparent *J* magnitude of 15 was used with a 300 s exposure. The spectral S/N were output in the *L* band to demonstrate `Imber`'s ability to scale apparent magnitudes based on input spectra and to demonstrate performance in a similar band as ELT/METIS. Vertical axis is logarithmic.

available to the instrument detector that can be converted to electrons.

To confirm `Imber`'s internal S/N calculator matches the ELT spectroscopic ETC, we directly compare their results for the same input in Figure 1. We input a 1500 K blackbody spectra with a *J*-band apparent magnitude of 15 along with an exposure time of 300 s. We output the spectral S/N in the *L* band to demonstrate `Imber`'s ability to scale instrument flux based on the input apparent magnitude's band and also to confirm this ability near the spectral range of an instrument such as ELT/METIS. `Imber`'s computed S/N closely matches the values calculated by ESO's ELT spectroscopic ETC, with small deviations primarily due to differences in sky transmission and emission models.

3. Methods

Using `Imber`, we predict the selected ELT instrument's ability to Doppler image ultracool targets. We begin by simulating observed LPs for each astronomical target; these observations are then fit via the analytical model described in Plummer & Wang (2022). As discussed in Plummer & Wang (2022) in greater detail, `Imber` can also be used to create light curves and infer surface inhomogeneities based solely on photometric data or in combination with spectroscopic data to provide a unified solution.

3.1. Simulating Observations

To provide simulated spectroscopic observations, we implement a numerical simulation for each astrophysical target. The target's gridded (250 latitude by 500 longitude) photosphere is first simulated using an appropriate limb-darkening effect to create a baseline flux map, which is the basis for the rotational broadening kernel (BK). For this paper, we select a linear limb-darkening law to lower computational costs based on Plummer & Wang's (2022) findings that rotational BKs created with linear and Claret coefficients agree within 2%.

Surface inhomogeneities are included via 2D Gaussian spots with positive (bright spots) or negative (dark spots) fluxes to create a time-varying spot map. In both numerical and analytical models, contrast can vary from twice the background brightness (contrast $= -1$) to a perfectly dark surface (contrast $= +1$). These 2D Gaussian spots are projected onto the orthographic view of the target (see Figure 2) from the observer's perspective via the Euler–Rodrigues formula (Shuster 1993), discussed in finer detail in Plummer & Wang (2022). After this coordinate transformation, summing the flux from each longitudinal column and interpolating onto the desired number of LP elements creates a BK incorporating both rotational broadening and spotted features.

With rapidly rotating objects, rotation is the dominant broadening mechanism. However, for slow rotators such as TRAPPIST-1, instrument, thermal, pressure, and natural broadening as well as microturbulence and macroturbulence can induce nonnegligible line broadening. To address this, for our template we adopt BT-Settl (Allard et al. 2012) spectral models for VLM stars and BDs (further discussed in Section 4.1), which use the PHOENIX stellar atmosphere code (Hauschildt 1992, 1993; Allard & Hauschildt 1995; Hauschildt et al. 1995; Hauschildt & Baron 1995; Baron et al. 1996; Hauschildt et al. 1996, 1997). This lineage of stellar models accounts for thermal broadening, pressure broadening, natural broadening, and microturbulence (Schweitzer et al. 1996). For instrument broadening, we assume a normalized Gaussian profile with a FWHM equal to the central wavelength divided by the resolving power of the spectrograph.

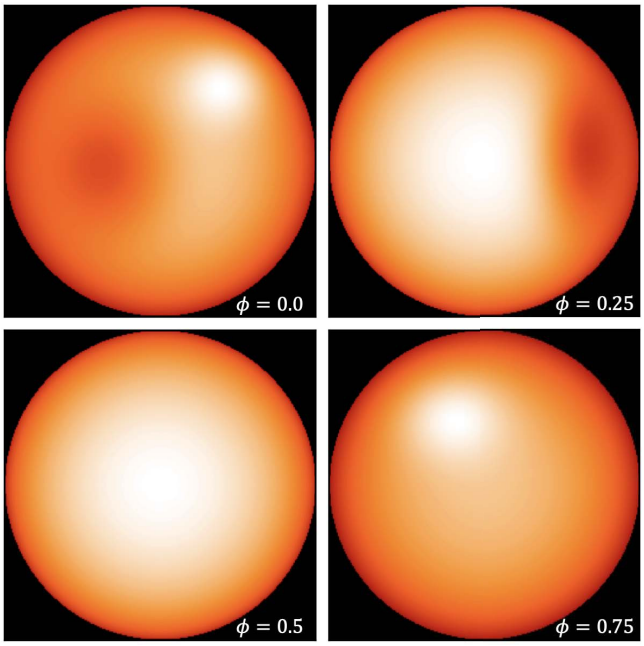

Figure 2. Orthographic view of example target ($i = 50°$) over a full rotation with phases of 0.0, 0.25, 0.5, and 0.75. Both a dark spot (latitude = 15°, radius = 30°, and contrast = 0.3) and bright spot (latitude = 60°, radius = 25°, and contrast = −0.2) are added to the surface. Flux field shown as implemented by `Imber` to numerically generate simulated spectra, LPs, and photometric light curves.

The rotational and instrument BKs are convolved with the astronomical target's BT-Settl model to create a noiseless synthetic spectrum. Figure 3 demonstrates the process of broadening template, synthetic spectra (BT-Settl) to model real-world spectroscopic observations. Fourteen NIR spectroscopic observations of Luhman 16B (originally published by Crossfield et al. 2014 and reprocessed in Luger et al. 2021) are overplotted by an appropriate BT-Settl model ($T = 1450$ K, log $(g) = 5.0$) both before and after rotational and instrument broadening. Similar results to those two works are achieved and shown.

It is at this stage that Gaussian noise is added to the spectrum to account for the simulated observation's S/N. As described in Section 2.4, the S/N depends on the selected target, instrument, and atmospheric conditions. In `Imber`, the S/N is computed at each wavelength, and the noise level is sampled at each epoch of observation to provide spectrally and temporally varying noise. At this point, we have a complete set of simulated spectra for mocked observations.

Adopting a realistic procedure, we use least-squares deconvolution (LSD), initially introduced by Donati et al. (1997) and refined by Kochukhov et al. (2010), to compute LPs for the simulated observed spectra. We use the following implementation of the technique as demonstrated in prior works (Wang et al. 2017, 2018a; Pai Asnodkar et al. 2022; Plummer & Wang 2022):

$$\boldsymbol{Z}(\upsilon_i) = (\boldsymbol{M^T} \cdot \boldsymbol{M} + \Lambda \boldsymbol{R})^{-1} \cdot \boldsymbol{M^T} \cdot \boldsymbol{Y}^0, \quad (2)$$

where $Z(\upsilon)$ is the LP and υ_i is the radial velocity corresponding to each element. M is a line mask Toeplitz matrix computed using a template spectrum as described in Donati et al. (1997). ΛR are the scalar regularization parameter and regularization Toeplitz matrix, which dampen noise amplification associated with LSD (Kochukhov et al. 2010; Donatelli & Reichel 2014).

3.2. Analytical Model

`Imber` analytically models the astronomical target as an instrumentally and rotationally broadened LP with scaled 1D Gaussian perturbations corresponding to surface inhomogeneities either adding or subtracting flux from the background profile. The residuals of this analytical model and the LSD-computed observed LP can be used to implement Bayesian inference on the spot parameters: latitude(s), longitude(s), radius(i), and contrast.

Bayesian retrieval with this technique will identify the most prominent surface features for the set number of spots. Typically, during analysis the number of spots is increased until the logarithmic evidence plateaus. Depending on the target's geometry and the data quality, degeneracies will begin to manifest as the number of spots retrieved increases. Gaussian priors can be implemented to break degeneracies but should be used with caution. For this reason, the computationally economical method summarized here and described in detail within Plummer & Wang (2022) should be thought to complement numerical cell-by-cell Doppler imaging with smoothing via maximum-entropy methods (Vogt et al. 1987) or Tikhonov regularization (Piskunov et al. 1990).

When applying this technique to real-world data, it may be necessary to account for additional broadening processes such as microturbulence or Doppler broadening (Gray et al. 2006). For these mechanisms, a convolution with an additional Gaussian BK whose width is determined either through Bayesian analysis or least-squares methods has been demonstrated to produce a reasonable fit (Plummer & Wang 2022).

3.3. Photometric Light Curves and Analytical Fit

As presented in Plummer & Wang (2022), `Imber` can also be used to both generate and fit photometric light curves. For the numerical simulation, the sum of the background photosphere flux is used to normalize to unity. That is, an unspotted surface will have a flux of 1. Bright spots add flux while dark spots subtract flux from the photometric curve. The analytical model works very similarly. The instrumental and rotational BK is used to normalize to unity such that the 1D Gaussian spots will either add or subtract from the light-curve flux. In this manner, `Imber` can both simulate observed light curves and fit those light curves with an analytical model, with similar caveats as the spectroscopic method with regards to degeneracies.

4. Application to Astronomical Targets

We will now apply our technique to six representative astronomical targets including TRAPPIST-1, VHS 1256 b, SIMP 0136, Beta Pic b, and HR 8799 d and e. A summary of each target's parameters pertinent to Doppler imaging are included in Table 2. Each target's apparent magnitudes, organized by photometric bands corresponding to instrument wavelength range, are summarized in Table 3. Because *I*-band magnitudes were not available for VHS 1256 b and SIMP 0136, we display the scaled *I*-band magnitude computed by `Imber` based on observed *J*-band magnitudes, their effective temperatures, and BT-Settl spectral models. The average computed S/Ns across each instrument's wavelength band

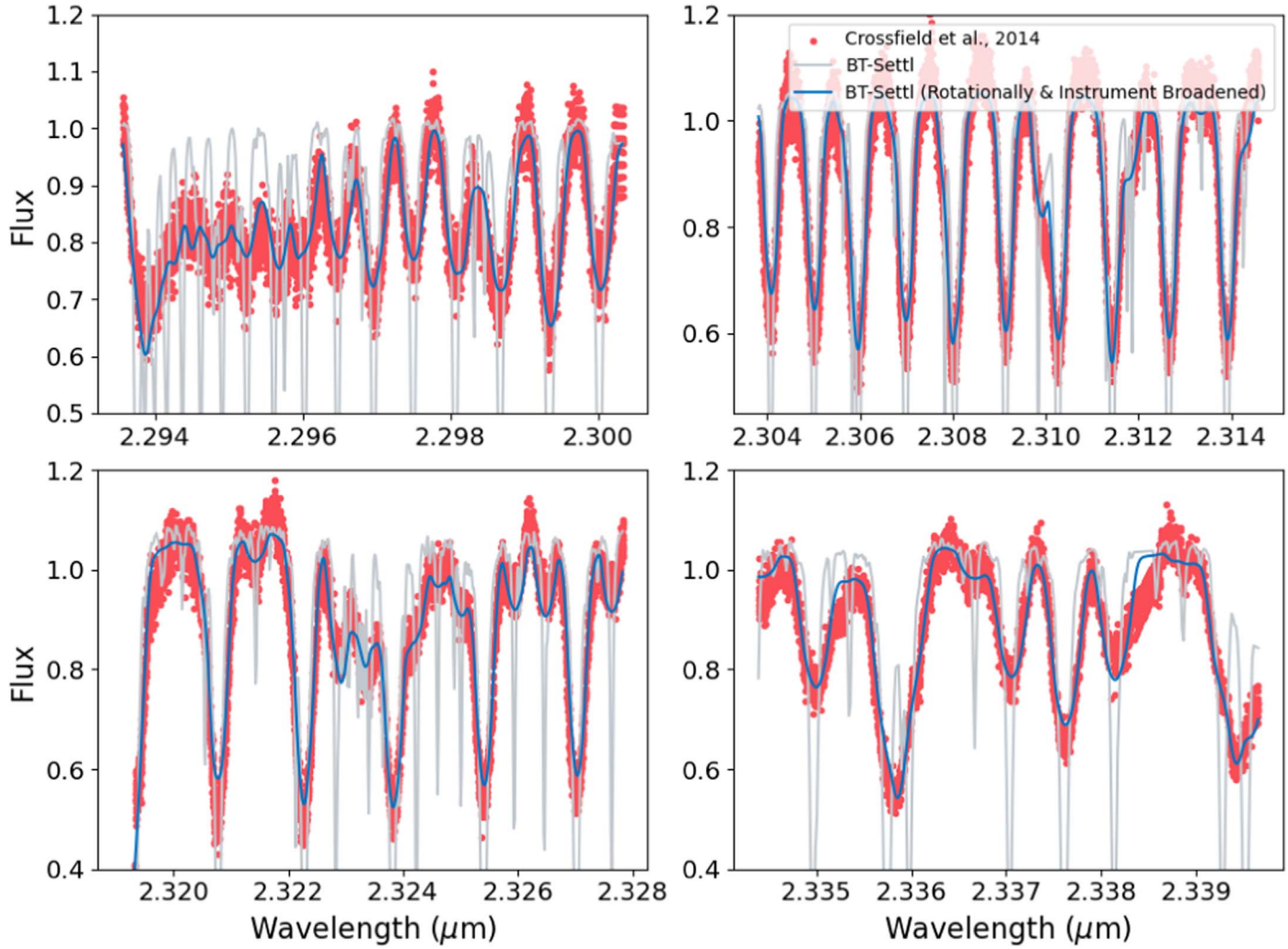

Figure 3. Demonstration of the rotational and instrument broadening (cyan) of a BT-Settl (Allard et al. 2012) model (gray) to fit real-world, Luhman 16B spectra (red). Luhman 16B observations were originally published by Crossfield et al. (2014) and reprocessed by Luger et al. (2021). Rotational BK assumes $v \sin i = 26.1$ km s^{-1} as per Crossfield et al. (2014).

are summarized numerically in Table 3 and graphically in Figure 4. Retrieved spot parameter uncertainties are shown in Figure 4.

4.1. Test Setup

We will test each instrument's (GMT/GCLEF, TMT/MODHIS, and ELT/METIS) ability to infer spot location and radius for a 1-Spot scenario. TMT/MODHIS and ELT/METIS will be applied to all six targets. Due to GMT/GCLEF's lack of first-light AO/HCI, it will not be applied to the companion EGPs (Beta Pic b and HR 8799 d and e). For both TMT/MODHIS and ELT/METIS, we conservatively assume 10^{-4} host star flux suppression, in agreement with estimates from the instrument literature (Mawet et al. 2019; Brandl et al. 2021).

Integrated exposure times (see Table 3) for each target are computed by dividing the object's period (see Table 2) by the number of samples. For our initial test, we adopt 15 samples, similar to Crossfield et al. (2014). A higher number of samples will improve temporal resolution at the cost of lower S/N, while the reverse is also true. These integrated exposure times are notional for objects with longer periods, as continuous viewing would not be feasible for periods $\gtrsim$10 hr.

Given the observed multirotational light-curve evolution seen in ultracool dwarfs (Buenzli et al. 2015a, 2015b; Zhou et al. 2020b, 2022), the temporal resolution may fail to capture the complete dynamic nature of spot parameters for slower rotators such as TRAPPIST-1 and VHS 1256 b. For this reason, dynamic spots with rotationally evolving size and contrast have been implemented in the `Imber` code and are planned to be the focus of a future work but are not included here to limit our scope.

As mentioned in Section 3.1, with all targets we adopt BT-Settl model spectra as described in Allard et al. (2012). These high-resolution template spectra include H_2O, CH_4, NH_3, and CO_2 opacity line lists, and revised solar oxygen abundances; in addition, they include cloud modeling, which allows the code to be applied to astrophysical objects with effective temperatures ranging from 400 to 70,000 K and a $\log(g)$ of -0.5 to 5.5 (Allard et al. 2012). These ranges match well with our intended ultracool targets.

For a fair comparison, we enforce the same input truth parameters (latitude = 30°, longitude = 30°, radius = 30°, and contrast = +0.25) across all targets. While the assumed values may not be representative for TRAPPIST-1's surface features (which are currently unknown), the values are typical for other

Table 2
Astronomical Target Parameters

Name (SpT)	$T_{\rm eff}$ (K)	log(g) (log(cm s^{-2}))	Inclination Posterior[a]	P (hr)	i (deg)	$v \sin i$ (km s^{-1})	Sources
TRAPPIST-1 (M8V[a])	2566 ± 26^{b}	$5.2396^{+0.0056}_{-0.0073}{}^{b}$		$\sim 79^{c,d}$	$\sim 90^{e}$	2.1 ± 0.3^{e}	[a]Costa et al. (2006) [b]Agol et al. (2021) [c]Luger et al. (2017) [d]Vida et al. (2017) [e]Brady et al. (2023)
VHS 1256 b (L7[a])	$\sim 1200^{b}$	$\sim 4.5^{b}$		22.04 ± 0.05^{c}	54^{+33}_{-39}	$13.5^{+3.6}_{-4.1}{}^{d}$	[a]Gauza et al. (2015) [b]Miles et al. (2023) [c]Zhou et al. (2020b) [d]Bryan et al. (2018)
SIMP 0136 (T2.5[a])	1150 ± 70^{b}	4.5 ± 0.4^{b}		2.425 ± 0.003^{c}	80^{+10d}_{-12}	$52.8^{+1.0d}_{-1.1}$	[a]Artigau et al. (2006) [b]Vos et al. (2023) [c]Artigau et al. (2009) [d]Vos et al. (2017)
Beta Pic b	1724 ± 15^{a}	4.18 ± 0.01^{a}		8.1 ± 1.0^{b}	57^{+18}_{-24}	25.0 ± 0.3^{b}	[a]Chilcote et al. (2017) [b]Snellen et al. (2014) [c]Bryan et al. (2020)
HR 8799 d	$1558.8^{+50.9a}_{-81.4}$	$5.1^{+0.3a}_{-0.4}$	Aligned Random	$6.0^{+2.5a}_{-1.5}$ $12.0^{+5.3}_{-4.4}$	24^{+14}_{-13} 51.0^{+42}_{-29}	$10.1^{+2.8a}_{-2.7}$	[a]Wang et al. (2021)
HR 8799 e	$1345.6^{+57.0a}_{-53.3}$	$3.7^{+0.3a}_{-0.1}$	Aligned Random	$4.1^{+1.1a}_{-0.8}$ $8.4^{+2.3}_{-3.0}$	24 ± 9 56^{+40}_{-22}	$15.0^{+2.3a}_{-2.6}$	[a]Wang et al. (2021)

Note.
[a] Two inclination prior scenarios are explored in Wang et al. (2021): (1) "Aligned," in which inclination priors are drawn based on the assumption that planetary spin inclination is aligned with orbital inclination; (2) "Random," in which inclination priors are drawn from a uniform distribution.

ultracool dwarfs in the literature. A radius of 30° agrees with inferred values for an equatorial dark spot on Luhman 16B from both Crossfield et al. (2014) and Plummer & Wang (2022). A contrast of +0.25 is consistent with spotted models fitting photometry for Luhman 16B (Karalidi et al. 2016; Plummer & Wang 2022) and VHS 1256 b (Zhou et al. 2022).

For Bayesian inference, we employ dynamic nested sampling (Skilling 2004, 2006; Higson et al. 2019) via the publicly available Python module `Dynesty` (Speagle 2020). For both spectroscopic and photometric Bayesian retrievals, we adopt uniform priors. Spot latitude and longitude distributions are $0° \pm 90°$ and $0° \pm 180°$, respectively. Radii distributions are uniform, with lower and upper bounds of 5° and 55°. For our instrument comparison, the contrast will be fixed at +0.25 (indicating a spot 25% darker than the background surface), but contrast as a free parameter is further explored in Section 5.

4.2. Application to TRAPPIST-1

4.2.1. TRAPPIST-1 Background

TRAPPIST-1 is a late M dwarf, hosting at least seven rocky exoplanets (Gillon et al. 2016, 2017), located 12.47 ± 0.01 pc (Gaia Collaboration et al. 2021) from our solar system. With a spectral type of M8V (Costa et al. 2006), TRAPPIST-1 has an effective temperature of $T_{\rm eff} = 2566 \pm 26$ K and a surface gravity of $\log(g) = 5.2396^{+0.0056}_{-0.0073}$ (Agol et al. 2021). Life would likely have had sufficient time to develop on the star's planets due to the system's estimated age of over 7 Gyr (Burgasser & Mamajek 2017), although this value is not without controversy as the star possesses conflicting spectral features and kinematics associated with both young stars and older, field main-sequence dwarfs, respectively (Gonzales et al. 2019).

Our interest in TRAPPIST-1 lies in its status as both a planetary host and an ultracool dwarf. Potentially three or four of the TRAPPIST-1 exoplanets lie within the star system's habitable zone (O'Malley-James & Kaltenegger 2017; Wilson et al. 2021), making it an exciting target for the search of extraterrestrial life. However, like many late M dwarfs, TRAPPIST-1 appears to be active, exhibiting solar flares (Vida et al. 2017; Paudel et al. 2018) as well as Hα (correlated with chromospheric activity; Reiners & Basri 2010) and X-ray and ultraviolet emissions (Wheatley et al. 2017). Starspots have been inferred in TRAPPIST-1's photosphere by several studies using K2 data (Luger et al. 2017; Morris et al. 2018). Bright spots appear to be correlated with flaring events (Morris et al. 2018), likely impacting the system's habitability and planetary atmospheric escape.

4.2.2. TRAPPIST-1 Setup and Results

As with TRAPPIST-1's age, until recently the star's rotational period also appeared to be unsettled in the literature. Reiners & Basri (2010) measured a $v \sin i$ of 6 ± 2 km s^{-1}, which aligned with the rotational period measurement of ~1.4 days from Gillon et al. (2016). However, photometric measurements using K2 and Spitzer data supported a rotational period of ~3.3 days, corresponding to a $v \sin i$ of ~1.8 km s^{-1} (Luger et al. 2017; Vida et al. 2017). The discrepancy was thought to be due to photometric observations recording the characteristic timescale of stellar activity versus the true rotational period (Roettenbacher & Kane 2017; Morris et al. 2018). Recent measurements from the extreme-precision radial-

Table 3
Apparent Magnitudes, Integration Times, and S/Ns

Name	GMT/GCLEF (I)	TMT/MODHIS (H)	ELT/METIS ($W1/L'$)	Integration Time (Aligned/Random)	Sources
TRAPPIST-1	14.024 ± 0.115[a]	10.718 ± 0.021[b]	10.067 ± 0.024[c] (W1)	5.28 h	[a]Costa et al. (2006) [b]Cutri et al. (2003) [c]Wright et al. (2010)
$S/N_{(avg)}$	229	1910	1640		
VHS 1256 b	~20.0 (computed)	15.595 ± 0.209[a]	13.6 ± 0.5[a] (W1)	1.46 h	[a]Gauza et al. (2015)
$S/N_{(avg)}$	7.39	97.7	53.5		
SIMP 0136	~16.6 (computed)	12.809 ± 0.002[a]	11.94 ± 0.02[b] (W1)	9.65 m	[a]Lawrence et al. (2012) [b]Cutri et al. (2014)
$S/N_{(avg)}$	13.1	118	79.0		
Beta Pic b	N/A	13.32 ± 0.14[a]	11.24 ± 0.08[a] (L-band)	32.4 m	[a]Currie et al. (2013)
$S/N_{(avg)}$	N/A	119	107		
HR 8799 d	N/A	17.29 ± 0.28[a]	14.59 ± 0.17[b] (L-band)	24/48 m	[a]Skemer et al. (2012) [b]Currie et al. (2014)
$S/N_{(avg)}$ (Aligned/Random)	N/A	8.13/11.6	4.33/6.14		
HR 8799 e	N/A	16.94 ± 0.28[a]	14.57 ± 0.23[b] (L-band)	16.4/33.6 m	[a]Skemer et al. (2012) [b]Currie et al. (2014)
$S/N_{(avg)}$ (Aligned/Random)	N/A	9.48/13.7	5.77/8.30		

velocity spectrograph MAROON-X suggest $v \sin i$ and period values of 2.1 ± 0.3 km s^{-1} and 3.3 days (Brady et al. 2023).

Due to TRAPPIST-1's assumed edge-on inclination ($i \sim 90°$), spot degeneracies are naturally created in the northern and southern hemispheres with respect to inferred latitude. Because the star's exact inclination is unknown, we will assume an inclination of 85° to provide a notional value to compute theoretical results.

Despite more than sufficient S/N, with TRAPPIST-1's $v \sin i$ of 2.1 km s^{-1} and the three instruments' spectral resolutions of $R \sim 100{,}000$, `Imber` is unable to sufficiently resolve deviations to the rotationally broadened LP to the degree required to successfully infer all spot parameters within 1σ. Although the retrieved longitude and radius were reasonably accurate, latitude retrievals possessed biases $\gtrsim$30°. Increasing the temporal resolution from 15 to 100 samples, per Kochukhov (2016), resulted in minor to negligible improvements to the retrieved solution.

To determine the source of the retrieved latitude inaccuracies, we explored varying TRAPPIST-1's stellar parameters. Decreasing the inclination to 45° and 60° improves the solution, but not enough to be within 1σ, with retrieved biases of ~5° and 10°, respectively. This result matches the Doppler imaging technique introduced in Hébrard et al. (2016) in which the injection-retrieval appears to have a retrieved a bias of ~10° for spots on a simulated target with $i = 60°$ and $v \sin i = 1$ km s^{-1}. However, by increasing $v \sin i$, it was determined that a $v \sin i \sim 7$ km s^{-1} resulted in a successful retrieval, with further improvement seen at higher $v \sin i$ values. Surveying NASA's Exoplanet Archive,[9] there are not currently any ultracool dwarfs with measured $v \sin i \gtrsim 3$ km s^{-1} hosting confirmed exoplanets.

[9] https://exoplanetarchive.ipac.caltech.edu/index.html

Provided polarimetric observations are available, Zeeman Doppler imaging (ZDI) offers the ability to map stellar magnetic structure, including starspots, for slower rotators. Such maps have been created for low $v \sin i$ (~1 to 4 km s^{-1}) targets including Sun-like stars (Petit et al. 2008) and early M dwarfs (Hébrard et al. 2016). ZDI might only be effective for the hottest ultracool objects as the enhanced magnetic activity associated with starspots has not yet been detected in objects cooler than L5 dwarfs (Paudel et al. 2018, 2020). In the future, we intend to extend our method to include deviations to polarized spectral LPs.

4.3. Application to VHS 1256 b

4.3.1. VHS 1256 b Background

VHS 1256 b is a PMO with mass $<20\,M_J$ near the L/T transition (L7 ± 1.5) discovered and initially characterized by Gauza et al. (2015). The ultracool dwarf orbits a binary M dwarf system at a distance of 179 ± 9 au (Dupuy et al. 2020). Notably, VHS 1256 b is a JWST Early Release Science (ERS) target. As part of ERS, Miles et al. (2023) presented the highest-fidelity spectrum of the object to date, with wavelength coverage ranging from 1 to 20 μm. In addition to identifying volatiles (H_2O, CH_4, CO, and CO_2) and alkali metals (Na and K) in VHS 1256 b's atmosphere, Miles et al. (2023) found strong spectral evidence for chemical disequilibrium, likely caused by vertical mixing, and achieved the first detection of silicate clouds in a planetary-mass companion.

Beyond chemical disequilibrium, atmospheric circulation is also suspected in VHS 1256 b due to its status as the most variable substellar object observed to date (Miles et al. 2023). Bowler et al. (2010, 2020) observed ~20% NIR spectroscopic variability using the Hubble Space Telescope's Wide Field Camera 3 (HST/WFC3). Follow-on studies using Spitzer's

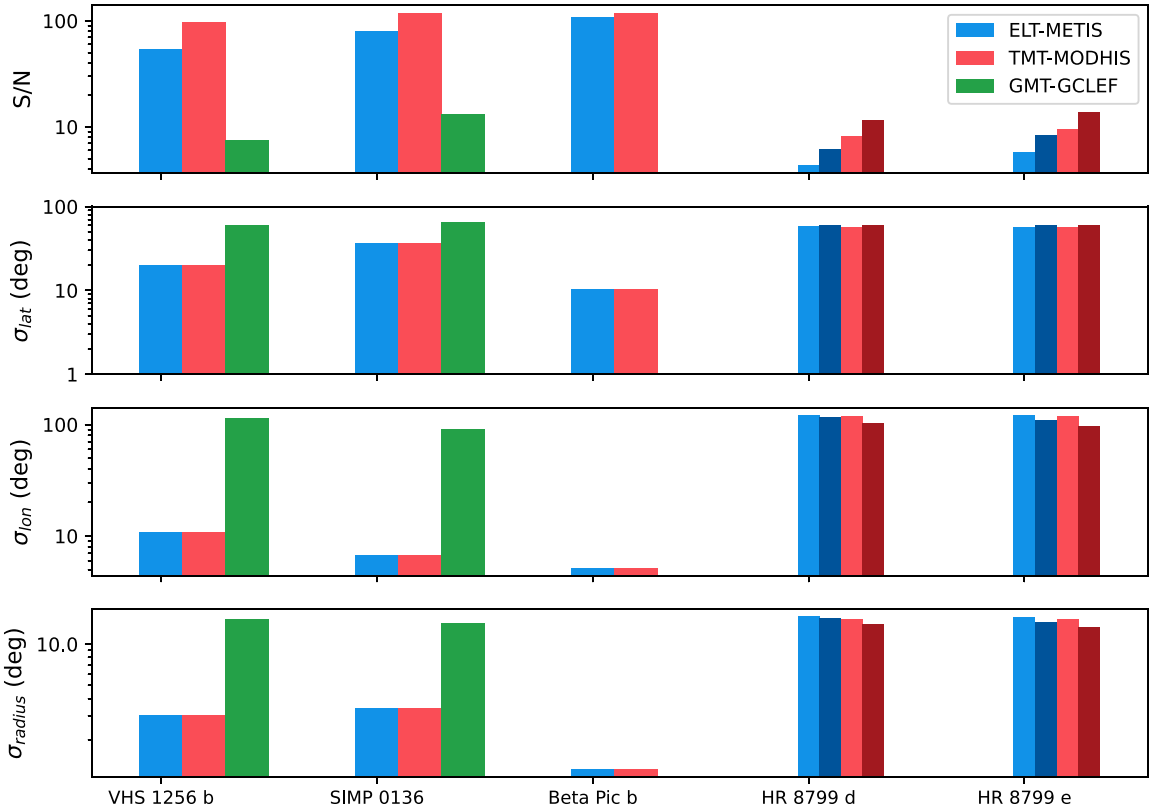

Figure 4. Computed S/Ns and retrieved latitude, longitude, and radius uncertainties (1σ) for each target. Each case assumes a 1-Spot model with latitude = 30°, longitude = 30°, radius = 30°, and a fixed contrast of +0.25, corresponding to a dark spot. For HR 8799 d and e, the lighter color bars denote retrievals run assuming inclinations aligned with the planets' orbital axes; darker bars denote inclinations derived from random uniform priors. All vertical axes are logarithmic. Retrievals conducted using `Imber` for numerical simulated observations and analytical model. `Dynesty` is used for dynamic nested sampling.

Infrared Array Camera's Channel 2 centered at 4.5 μm (Zhou et al. 2020b) and the HST J band (Zhou et al. 2022) detected variability of $5.76\% \pm 0.04\%$ and up to 38%, respectively. As discussed in Zhou et al. (2020b), substellar models (Marley et al. 2010; Morley et al. 2014) predict variability to be larger at shorter wavelengths and deeper atmospheric levels than at longer wavelengths corresponding to molecular bands.

4.3.2. VHS 1256 b Setup and Results

Studies have inferred a range of temperatures for VHS 1256 b from 1000 to 1380 K (Zhou et al. 2020a; Hoch et al. 2022; Dupuy et al. 2023; Miles et al. 2023; Petrus et al. 2023). For the BT-Settl template, we use an effective temperature of 1200 K as a compromise and $\log(g) = 4.5$ from Miles et al. (2023). In terms of rotation, we adopt a period of 22.04 ± 0.05 hr (Zhou et al. 2020b) and $v \sin i = 13.5^{+3.6}_{-4.1}$ km s^{-1} from Bryan et al. (2018). Using this value, along with the inferred equatorial speed, $v_{\rm eq} = 16.6^{+5.8}_{-7.0}$ km s^{-1} from Bryan et al. 2020, we compute an inclination of $54^{\circ}{}^{+33\circ}_{-39\circ}$ by assuming the following expression:

$$i = \sin^{-1}\left(\frac{v \sin i}{v_r}\right). \quad (3)$$

We apply the same method for targets with unpublished inclinations such as Beta Pic b and the HR 8799 planets.

To demonstrate the process used for each target, VHS 1256 b will be used as an example. Figure 5 is a corner plot showing the posterior distributions for the spot latitude, longitude, and radius for mocked observations using ELT/METIS. For each parameter, the input value is within the 68% credible range. Using the solution with the greatest likelihood, we generate LPs to compare the inferred analytical model to the the synthetic LP deviations created with our numerical simulation. The results can be seen in Figure 6 with our simulated observation, inferred model (reduced $\chi^2 = 0.844$), and residuals.

The residuals in Figure 6 appear to approximate Gaussian white noise. To confirm this, we plot the residual distribution in Figure 7. The residuals approach a Gaussian distribution with a fit producing an approximately zero mean and a standard deviation ($\sigma = 0.00224$) corresponding to a LP S/N ~450, a factor of 8 gain over the mean spectra S/N (~55). Due to its broader wavelength coverage, TMT/MODHIS shows an even more significant gain (factor of 16) between mean spectral and LP S/N (~100 to ~1600, respectively). The S/N gain scales with the square root of the number of deep absorption lines (which can be estimated by the wavelength coverage). Expectations are met as the gain for TMT/MODHIS ($\Delta\lambda = 1450$ nm) is approximately twice that of ELT/METIS ($\Delta\lambda = 300$ nm).

TMT/MODHIS and ELT/METIS provide an order of magnitude greater mean spectra S/N than GMT/GCLEF, as is expected based on each telescopes' relative aperture size and wavelength coverage with regard to predominantly IR targets. The corresponding retrieved latitude, longitude, and radius uncertainties can be seen in Figure 4. TMT/MODHIS provides improved S/N over ELT/METIS (~100 versus ~55), likely due to the enhanced thermal background in ELT/METIS's L

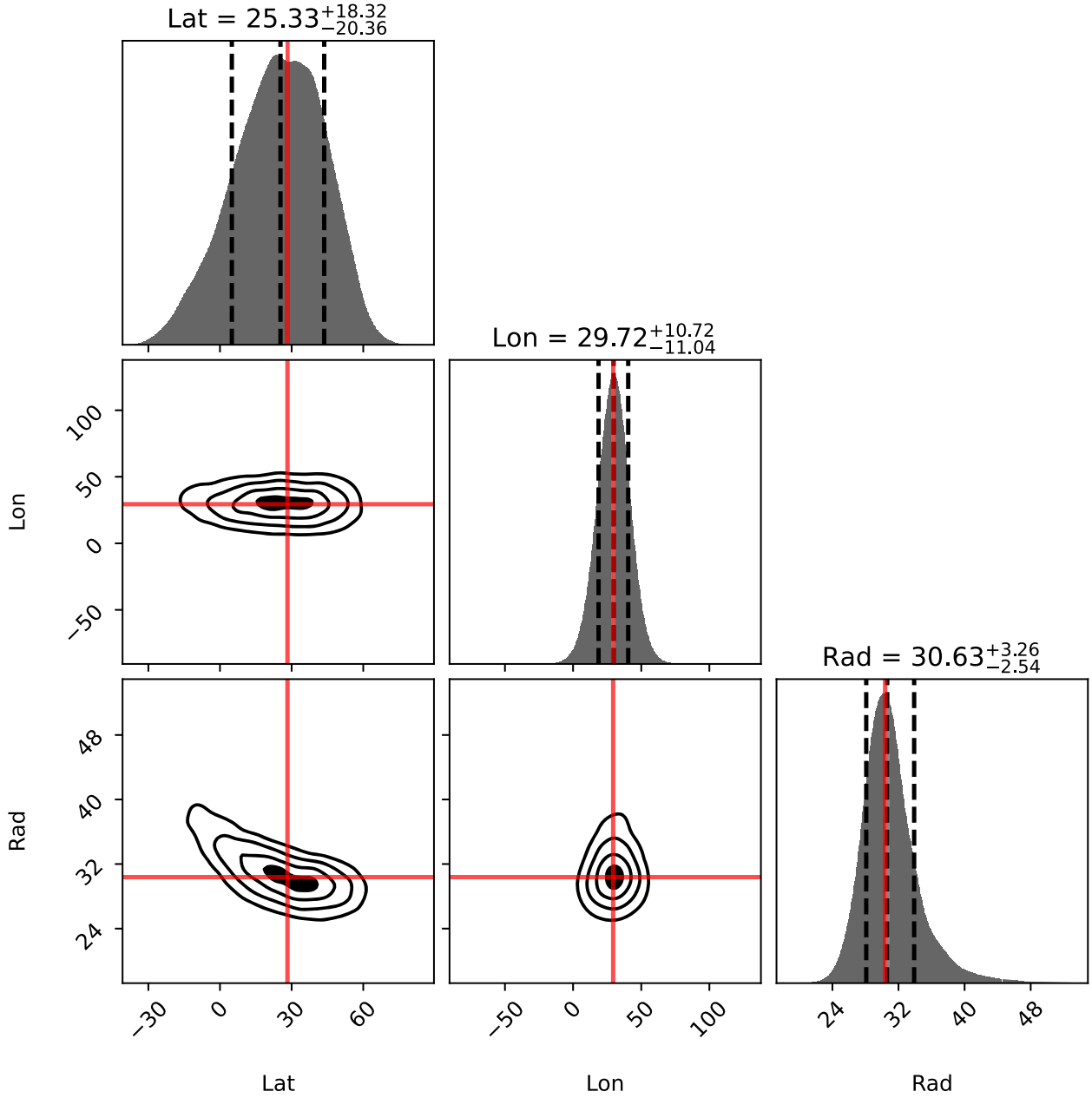

Figure 5. VHS 1256 b example Bayesian retrieval of 1-Spot scenario with ELT/METIS via dynamic nested sampling. The mean inferred values along with 1σ quantiles are displayed on the top of each column. Contours denote 0.5, 1, 1.5, and 2σ regions. Truth values are shown by the red line. Plot created with `Dynesty` (Speagle 2020).

band, but this only results in a small difference in resulting uncertainties.

For TMT/MODHIS and ELT/METIS, latitude uncertainties are approximately 2 to 10 times higher than longitude and radius uncertainties. Difficulties with inferring latitude (versus longitude, size, or contrast) via Doppler imaging have been documented (Khokhlova 1985; Khokhlova et al. 1986; Vogt et al. 1987), and stems from the more subtle LP deviations that need to be resolved to precisely infer spot latitude.

4.4. Application to SIMP 0136

4.4.1. SIMP 0136 Background

Similar to VHS 1256 b, SIMP 0136 (T2±0.5; Artigau et al. 2006) is an ultracool object at the L/T transition with a mass ($12.7 \pm 1.0\,M_J$; Gagné et al. 2017) near the deuterium-burning mass limit. First discovered by Artigau et al. (2006), SIMP 0136 was previously considered to be a higher-mass BD, but due to its likely (>99.9%) membership in the Carina-Near moving group (Gagné et al. 2017) and corresponding age (200 ± 50 Myr; Zuckerman et al. 2006), its mass appears to be that of a PMO (sometimes denoted as a rogue planet).

Significant *J*-band photometric variability has been detected for SIMP 0136. Artigau et al. (2009) first detected a peak-to-peak amplitude variability of 8% with a rotational period of ~2.4 hr. Follow-up observations by Radigan et al. (2014) saw smaller amplitudes of 2.9% but did not capture a full period. Croll et al. (2016) performed observations over 15 nights and found variability to evolve from <1% to >6% on timescales of one to 10 rotational periods. More recent observations by

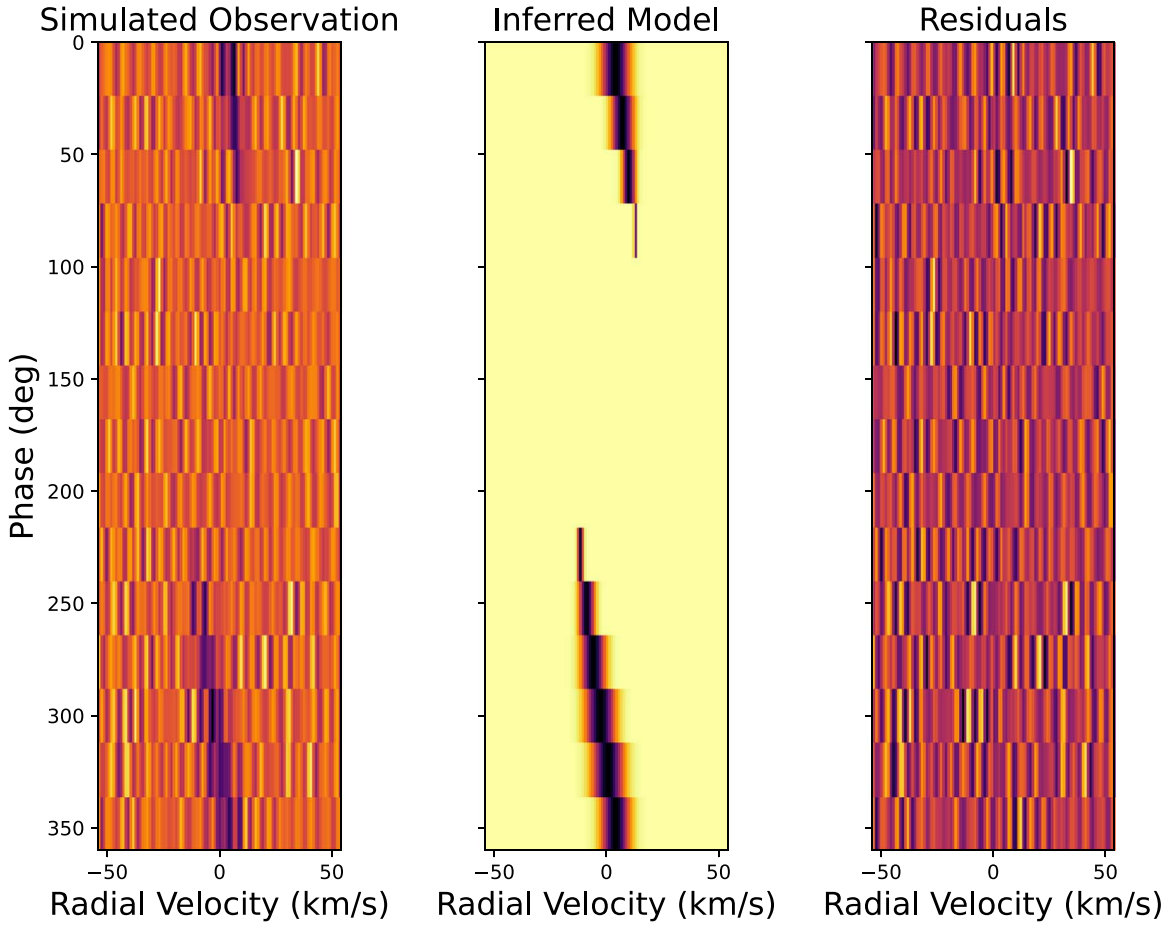

Figure 6. VHS 1256 b LP deviations. Left: deviations from simulated ELT/METIS observations. Middle: modeled deviations (reduced $\chi^2 = 0.844$) for inferred dark spot. Right: residuals computed by subtracting modeled LP deviations from observed LP deviations.

Eriksson et al. (2019) confirmed strong variability. A two-layer model comprised of a cold, upper layer and hot, deeper level has been proposed (Apai et al. 2013) and demonstrated (Yang et al. 2016) to explain SIMP 0136's variability. Recently, Vos et al. (2023) found that observations best match overlying, patchy forsterite clouds and a deeper, thick iron cloud deck.

4.4.2. SIMP 0136 Setup and Results

Astronomical parameters (see Table 2) for SIMP 0136 necessary for selecting a BT-Settl spectral model ($T_{\rm eff}$, $\log(g)$) and relevant to Doppler imaging ($v \sin i$, i) are explored in Gagné et al. (2017) and Vos et al. (2017, 2023). For effective temperature and surface gravity, we adopt the latest estimates from Vos et al. (2023): $T_{\rm eff} = 1150 \pm 70$ K and $\log(g) = 4.5 \pm 0.4$. Gagné et al. (2017) constrains the $v \sin i = 50.9 \pm 0.8$ km s^{-1} and inclination, $i = 55.9° \pm 0.8°$. Vos et al. (2017) finds a similar $v \sin i$ ($52.8^{+1.0}_{-1.1}$ km s^{-1}), but a higher inclination ($80°^{+10°}_{-12°}$). We adopt the Vos et al. (2017) values due to the more conservative (for Doppler imaging) inclination. SIMP 0136 has a measured rotational period of 2.425 ± 0.05 hr (Artigau et al. 2009).

The S/N and retrieved parameter uncertainties for SIMP 0136 are qualitatively alike to VHS 1256 b, with the exception of latitude uncertainty. The retrieved latitude uncertainty for SIMP 0136 is approximately twice that of VHS 1256, a result likely due to SIMP 0136's near edge-on inclination and the degeneracies created by this geometry. A similar but lesser effect is seen in SIMP 0136's retrieved radius when compared to the VHS 1256 b results. Small improvements to SIMP 0136's longitude (not affected by high inclination) are due to its higher S/N.

4.5. Application to Beta Pic b

4.5.1. Beta Pic b Results

Beta Pic is a 24 ± 3 Myr (Bell et al. 2015) star system located relatively close to our own solar system at 19.44 ± 0.05 pc in the aptly named Beta Pic moving group (van Leeuwen 2007). It is host to Beta Pic b, a directly imaged EGP with favorable contrast to its host star due to its youth and large, though disputed, mass ($\sim$10 to 15 M_J; Lagrange et al. 2010, 2012; Bonnefoy et al. 2013, 2014; Morzinski et al. 2015; Chilcote et al. 2017; Snellen & Brown 2018; Dupuy et al. 2019; Kervella et al. 2019; GRAVITY Collaboration et al. 2020; Lagrange et al. 2020; Vandal et al. 2020; Brandl et al. 2021). Notionally identified in Lagrange et al. (2009) and then confirmed by Lagrange et al. (2010), Beta Pic b orbits its host star with a semimajor axis of 9.8 ± 0.4 au (Lagrange et al. 2020).

4.5.2. Beta Pic b Setup and Results

For our spectral template, we reference the effective temperature and surface gravity inferred by Chilcote et al. (2017; $T_{\rm eff} = 1724 \pm 15$ K, $\log(g) = 4.18 \pm 0.01$) and

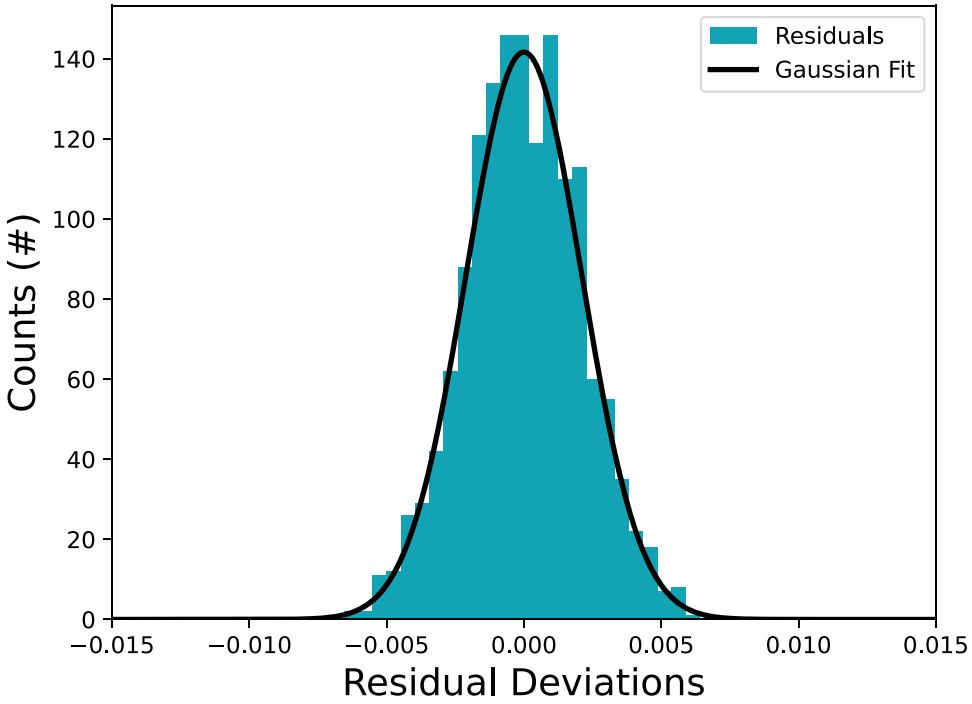

Figure 7. Residuals distribution of simulated VHS 1256 b LP deviations (for ELT/METIS) and inferred analytical model. Distribution is fit with Gaussian profile resulting in $\mu = -4.85 \times 10^{-7}$ and $\sigma = 0.00224$. The LP noise level corresponds to a S/N $\sim$ 450, a significant increase over the mean spectral S/N ($\sim$55). With a wider spectral band, TMT/MODHIS shows even higher gain with S/N improvement of $\sim$100 to $\sim$1600. As the S/N gain scales with the square root of the number of deep absorption lines (with wavelength coverage as a proxy), expectations are met as TMT/MODHIS (gain = 16, $\Delta\lambda = 1450$ nm) results in twice the S/N gain as ELT/METIS (gain $\sim$8, $\Delta\lambda = 300$ nm). Although the distribution is only approximately Gaussian in the figure, tests indicate increasing time samples leads to convergence on the Gaussian.

GRAVITY Collaboration et al. (2020; $T_{\rm eff} = 1742 \pm 10$ K, $\log(g) = 4.34^{+0.08}_{-0.09}$) to select a BT-Settl model with $T_{\rm eff} = 1700$ K and $\log(g) = 4.0$. Beta Pic b has an observed period of 8.1 ± 1.0 hr and $\upsilon \sin i$ of 25.0 ± 3.0 km s^{-1} (Snellen et al. 2014). Similar to how we proceeded for VHS 1256 b, we can use Beta Pic b's rotational velocity, $29.7^{+6.1}_{-8.8}$ km s^{-1} (Bryan et al. 2020) and $\upsilon \sin i$ to compute its inclination, $57^{\circ}{}^{+18\circ}_{-24\circ}$.

For a directly imaged EGP, Beta Pic b is relatively bright, which is reflected in its larger S/N and smaller retrieved parameter uncertainties than the more massive L/T transition ultracool objects (VHS 1256 b and SIMP 0136). As mentioned above, we conservatively assume both TMT/MODHIS and ELT/METIS suppress starlight with a contrast of 10^{-4}. Actual contrast values are likely to be improved in the final instrument design; however, starlight contamination above these levels would degrade the predicted performance.

4.6. Application to HR 8799 d and e

4.6.1. HR 8799 d and e Background

HR 8799 is a young star system with an estimated age of 30^{+20}_{-10} Myr (Doyon et al. 2010; Zuckerman et al. 2011) derived from its likely membership within the Columba association moving group. HR 8799 hosts at least four EGPs (Marois et al. 2008, 2010), inner and outer debris disks (interior to HR 8799 e and exterior to HR 8799 b), and a halo consisting of small dust grains (Su et al. 2009). The two innermost detected planets in the system to date, at $\sim$24 and 15 au, respectively (Marois et al. 2008, 2010; GRAVITY Collaboration et al. 2019), HR 8799 d and e likely have masses between 7 and 10 M_J (Marois et al. 2008, 2010; Wang et al. 2018b; GRAVITY Collaboration et al. 2019).

Clouds and chemical disequilibrium appear to be prevalent among the gas giant planets of HR 8799. Within the outer three planets (HR 8799 bcd), observations indicate the likely presence of clouds and chemical disequilibrium (Bowler et al. 2010; Hinz et al. 2010; Janson et al. 2010; Barman et al. 2011; Madhusudhan et al. 2011; Marley et al. 2012; Currie et al. 2014, 2014; Skemer et al. 2014; Barman et al. 2015; Bonnefoy et al. 2016; Lavie et al. 2017; Wang et al. 2020; Ruffio et al. 2021; Wang et al. 2022a, 2022b). Furthermore, Marley et al. (2012) presents evidence that patchy cloud models fit HR 8799 bcd observations, and Currie et al. (2014) argues that all four gas giants' photometry fit thick, patchy cloud models better than uniform cloud models. Chemical disequilibrium and thick clouds have also been inferred in HR 8799 e in relatively recent literature (Bonnefoy et al. 2016; GRAVITY Collaboration et al. 2019; Mollière et al. 2020).

4.6.2. HR 8799 d and e Setup and Results

For HR 8799 d's and e's effective temperature ($1558.8^{+50.9}_{-81.4}$ K/$1345.6^{+57.0}_{-53.3}$ K) and logarithmic surface gravity ($5.1^{+0.3}_{-0.4}$ /$3.7^{+0.3}_{-0.1}$), we adopt values retrieved by Wang et al. (2021) using BT-Settl models. As discussed in Wang et al. (2021), these temperatures and HR 8799 d's surface gravity are higher than the values cited in the preponderance of studies (Marois et al. 2008, 2010; Bonnefoy et al. 2016; Greenbaum et al. 2018; Wang et al. 2022b). However, because we are also using BT-Settl models for our templates due to their high resolution, we cautiously adopt Wang et al.'s (2021) values.

The spin parameters for both HR 8799 d and e derive from Wang et al. (2021), in which two inclination scenarios are

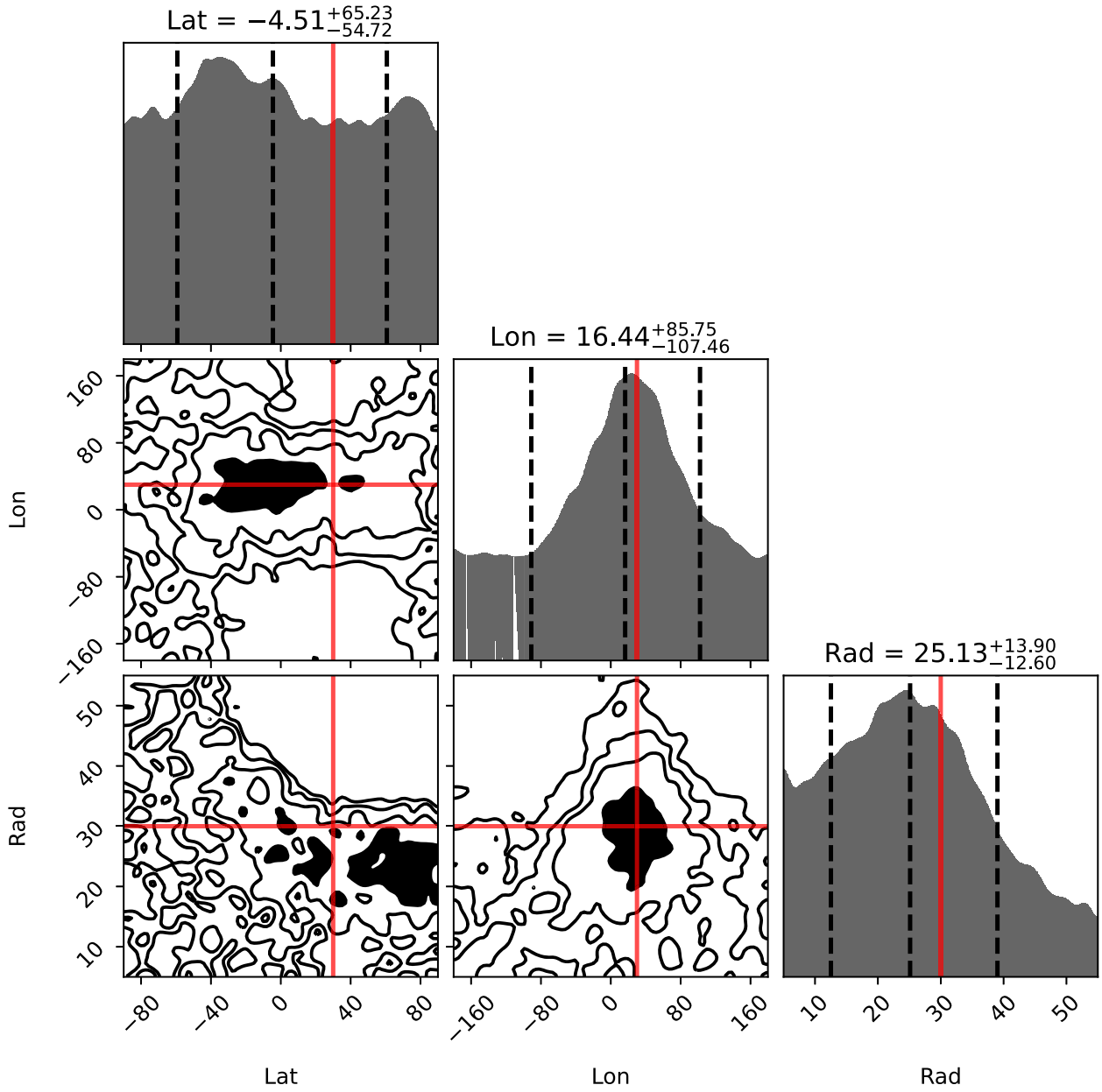

Figure 8. HR 8799 e (random prior inclination, one rotation) Bayesian retrieval of 1-Spot scenario with TMT/MODHIS via dynamic nested sampling. The mean inferred values along with 1σ quantiles are displayed on the top of each column. Contours denote 0.5, 1, 1.5, and 2σ regions. Truth values are shown by the red line. Plot created with `Dynesty` (Speagle 2020).

considered: the first, in which inclination priors are based on the orbital inclination ($\sim$26°; Wang et al. 2018b; Goździewski & Migaszewski 2020), and the second, in which the inclination priors derive from a random uniform distribution of $v \sin i$ as in Bryan et al. (2020). These assumptions lead to varying periods, computed inclinations (see Table 2), and, ultimately, integration times (see Table 3). Wang et al. (2021) infers $v \sin i$ values of $10.1^{+2.8}_{-2.7}$ km s^{-1}/$15.0^{+2.3}_{-2.6}$ km s^{-1} for HR 8799 d and e.

Due to the faint apparent magnitudes of HR 8799 d and e, the planets have the lowest S/Ns and highest average uncertainties out of the targets evaluated with TMT/MODHIS and ELT/METIS. The "random" inclination scenarios result in longer periods (with fixed temporal sampling this means longer integration times) and more edge-on viewing angles. As a result, these scenarios yield comparatively higher S/Ns and overall more constrained parameters than when their inclinations are aligned with their orbits.

Figure 8 demonstrates that, although the uncertainties are high, longitude and radius are beginning to be constrained for one rotation. Simulating five rotations and stacking the integrated exposures (S/N $\sim$31 for TMT/MODHIS) leads to all three parameters being constrained (see Figure 9). Although this technique would not identify atmospheric evolution on the timescales observed for the most variable ultracool dwarfs (VHS 1256 b, SIMP 0136, etc.), it would likely identify enduring features such as Jupiter's Great Red Spot. It should be noted observations over five rotations would require a significant investment in observation time.

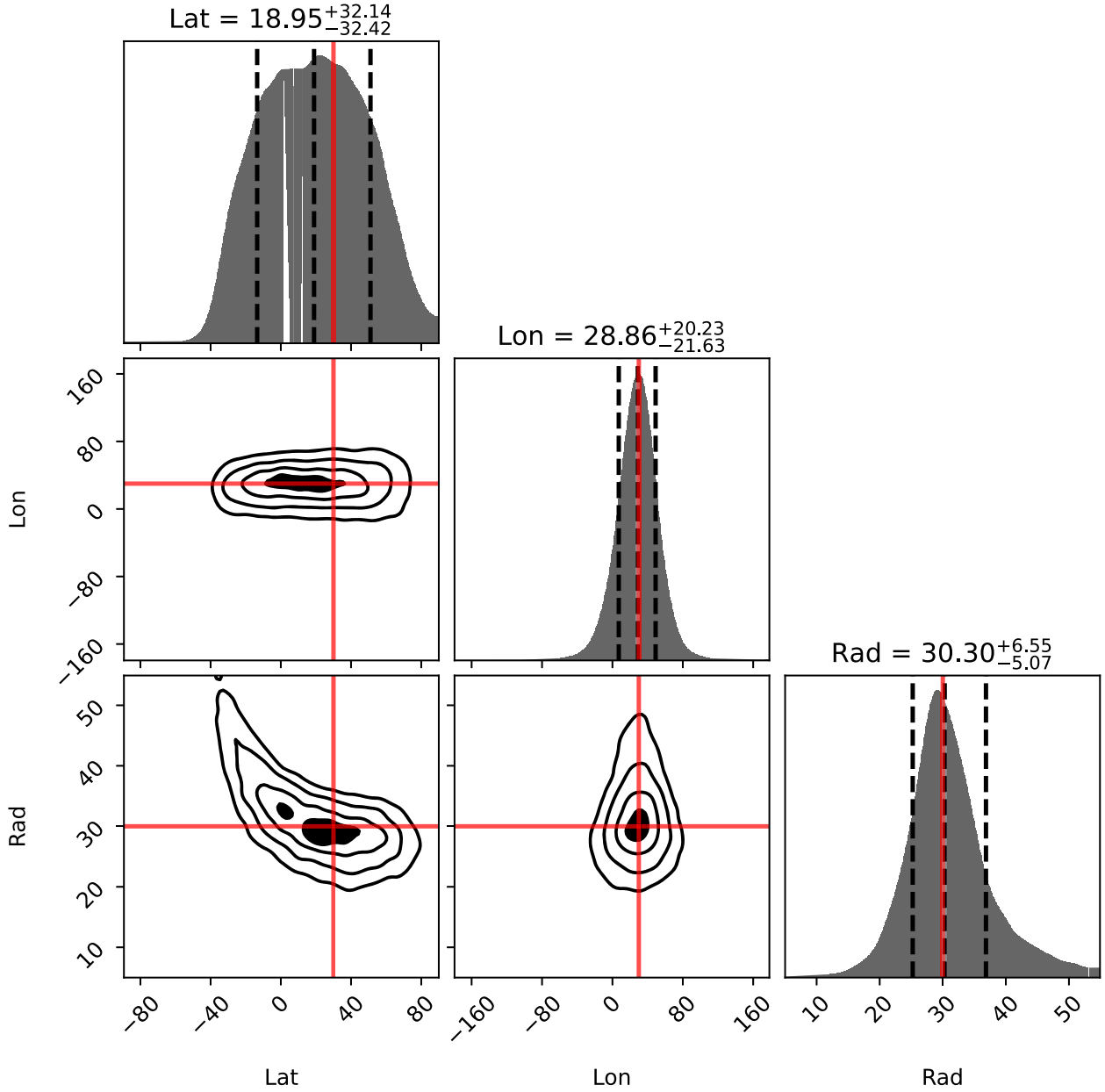

Figure 9. HR 8799 e (random prior inclination, five rotations) Bayesian retrieval of 1-Spot scenario with TMT/MODHIS via dynamic nested sampling. The mean inferred values along with 1σ quantiles are displayed on the top of each column. Contours denote 0.5, 1, 1.5, and 2σ regions. Truth values are shown by the red line. Plot created with `Dynesty` (Speagle 2020).

5. Improved Doppler Imaging Performance by Combined Spectroscopy/Photometry

Near-simultaneous, multimodal observations have proven to be beneficial in astronomical observations (Albrecht et al. 2022). As demonstrated in Plummer & Wang (2022), the framework used in `Imber` can be used to generate both synthetic spectroscopic and photometric data via numerical simulation and also infer spot location, size, and contrast with computationally inexpensive analytical modeling using both spectral LPs and photometric light curves.

As discussed in Section 2.3, ELT/METIS has both IFU spectrograph and imaging modes. Here both modes are applied to VHS 1256 b (with properties as described in Section 4.3) to compare each mode's ability to retrieve spot parameters. We also consider a near-simultaneous, combined spectroscopic and photometric observation.

5.1. Test Setup

Simulating ELT/METIS's imaging mode is conducted very similarly to the spectroscopic mode described in Section 2.4. An airmass of 1.5 is assumed at Cerro Armazones. To improve inference using light curves, the number of time samples is increased from 15 to 30. For photometry, an exposure time of 60 s is used, resulting in a S/N $\sim$ 1830, considerably higher than those achieved with the spectroscopic instruments.

Increasing the number of time samples reduces each spectroscopic exposure (from 1.46 hr to 44 minutes) and corresponding S/N (from $\sim$53 to $\sim$38), but enhances temporal resolution. When spectroscopy is combined with photometry, the integrated time for spectroscopy is 43 minutes per exposure (as 60 s is used for photometry) with minimal impact on the resulting spectroscopic S/N ($\sim$37).

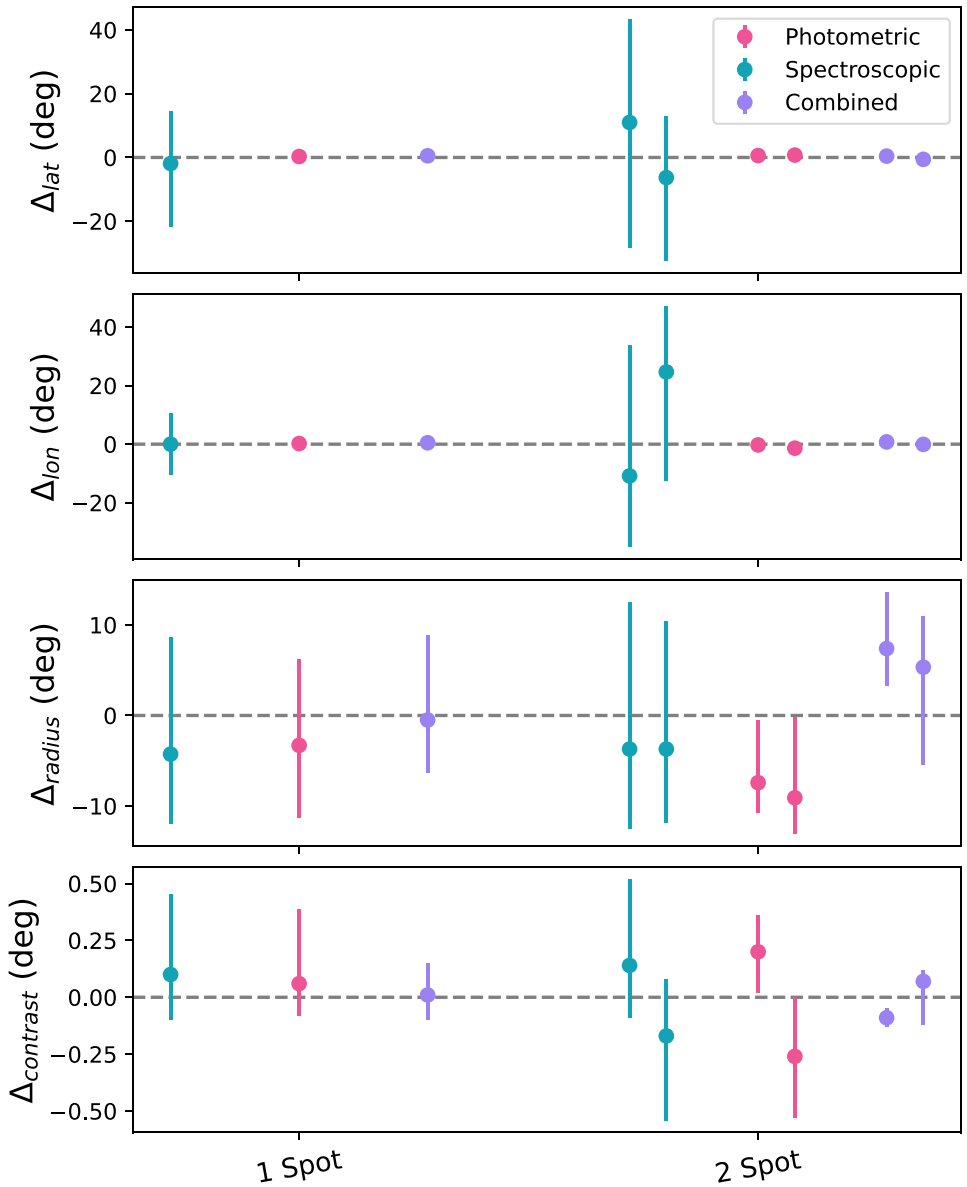

Figure 10. VHS 1256 b retrieval results for spectroscopic (aqua), photometric (magenta), and combined spectroscopic/photometric (indigo) modes. Spectroscopy and photometry are conducted with ELT/METIS's IFU and *L*-band imager, respectively. Central point depicts maximum likelihood value and error bars represent 1σ uncertainty. For the 2-Spot model, for each mode the left error bar corresponds to the input dark spot and the right value corresponds to the input bright spot. Vertical axes show retrieved deviations from input truth values.

For this test, we consider two cases: Case 1 with one dark spot (lat. $= 30°$, lon. $= 30°$, radius $= 30°$, contrast $= +0.25$) and Case 2 with two spots, bright and dark (lat. $= 30°$, $60°$, lon. $= -60°$, $60°$, radius $= 30°$, $30°$, contrast $= +0.25$, -0.25). Latitude, longitude, radius, and contrast are free parameters in all scenarios. Each retrieval's deviations from the input truth parameter is shown in Figure 10.

For the 1-Spot models, the contrast priors vary uniformly from $+1.0$ to -1.0, but for the 2-Spot model priors, we use both a bright spot (-0.5 ± 0.5) and dark spot ($+0.5 \pm 0.5$). All other priors are as described in Section 4.1.

5.2. Combined Spectroscopy/Photometry Results

Incorporating photometry into the retrieval results in improved inferred values in nearly all scenarios. For 1-Spot models, although photometry alone improves both the retrieval's accuracy and uncertainty, a combined spectroscopic/photometric solution is even better. The 2-Spot model introduces a more complicated picture. Photometry-alone observations introduce a bias in the retrieved radius and contrast which is not fully resolved in the combined solution. These biases could perhaps be addressed by weighting the spectroscopic observations higher in the combined solution.

5.3. Opportunities from Combined Spectroscopy and Photometry

Ongoing tension exists as to whether the spectral and photometric variability seen near the L/T transition is primarily due to planetary waves within banded structures or spotted features such as vortices, cloud systems, and rain-out patches. Apai et al. (2017) and Apai et al. (2021) argue the former case based on long-term photometric observations of ultracool dwarfs. Polarimetric observations of the binary BD system, Luhman 16, also support banding

(Millar-Blanchaer et al. 2020). There is furthermore a growing consensus in the BD general circulation model community that atmospheric zonal bands form in nearly all radiative and convective forcing scenarios, even if only in the form of a single equatorial jet (Zhang & Showman 2014; Showman et al. 2019).

On the other hand, there may also be a strong argument in favor of spotted features driving the observed variability and color and magnitude behavior at the L/T transition (Ackerman & Marley 2001). Recent analysis by Zhou et al. (2022) of VHS 1256 b multirotational photometry identified a degeneracy where both wave- and spot-based models could dictate rotational modulation in ultracool objects. Furthermore, Crossfield et al. (2014) inferred and mapped spotted features on the visible surface of Luhman 16B using spectroscopy-based Doppler imaging, a technique insensitive to planetary banding. These results were replicated in Luger et al. (2021) and Plummer & Wang (2022).

Using a combined spectroscopic and photometric approach, we could break this degeneracy and gain greater insight into the atmospheric structure of ultracool dwarfs and EGPs. Spectroscopic observations can confirm the existence and number of spotted features deforming a spectral LP for a specific astrophysical target. Furthermore, based on our results in Section 5.2 and shown in Figure 10, it can be seen that supplementing spectroscopic observations with near-simultaneous photometry has the potential to improve spot inference. This proposed technique would be ideal for either coordinated efforts between observatories or instruments such as ELT/METIS that contain both spectroscopic and imaging modes.

6. Summary

We have applied the unified spectroscopic and photometric numerical and analytical model developed in Plummer & Wang (2022) to estimate Doppler imaging performance for ELT instruments using our publicly available Python code `Imber`. We simulated spectral LPs for six targets including a VLM star (TRAPPIST-1), two ultracool dwarfs (VHS 1256 b and SIMP 0136), and three directly imaged exoplanets (Beta Pic b and HR 8799 d and e). With dynamic nested sampling, we performed *injection-retrieval* for surface inhomogeneities, inferring spot parameters via our analytical method. Our primary findings are as follows:

1. TMT/MODHIS and ELT/METIS are suitable instruments for Doppler imaging VHS 1256 b, SIMP 0136, and Beta Pic b over one rotation. HR 8799 d and e may require multiple rotations with stacked spectra.
2. GMT/GCLEF results in uncertainties significantly greater than TMT/MODHIS and ELT/METIS for the selected targets due to its wavelength coverage and aperture size. Stacking multiple rotation observations could allow for the identification of surface features using GMT/GCLEF.
3. TRAPPIST-1 appears to be a less suitable target for all three instruments due to its relatively low $v \sin i$ ($2.1\ \mathrm{km\ s^{-1}}$) and near edge-on inclination ($i \sim 90°$). With a notional 85° inclination, tests indicate $v \sin i$ values of $\gtrsim 7\ \mathrm{km\ s^{-1}}$ are required to successfully retrieve spot parameters.
4. Instruments with both spectroscopic and imaging modes, such as ELT/METIS, may be able to improve their solutions by augmenting spectroscopic data with short-exposure-time photometry.

Moving forward, `Imber` can provide an estimation of spectroscopic and photometric instruments' abilities to detect magnetic spots, cloud structures, and storm systems in stars and ultracool objects to address questions such as habitability and the exact nature of the spectral L/T transition. The code can also be applied to real-world observations to detect surface inhomogeneities, as demonstrated in Plummer & Wang (2022). In terms of future astrophysical applications, the unified spectroscopic and photometric approach of `Imber` makes it particularly well suited to solve problems such as the degeneracy between spotted features and planetary banding seen in long-term ultracool object photometry.

Acknowledgments

The authors would like to thank the United States Air Force Academy, Department of Physics for sponsoring the graduate work of the first author. Additionally, we want to acknowledge the instrument expertise and guidance of Bernhard Brandl, Jochen Liske, Dimitri Mawet, and Andrew Szentgyorgyi. We want to thank the anonymous referee for constructive feedback and suggestions during the review process. We would like to thank the Group for Studies of Exoplanets (GFORSE) at The Ohio State University, Department of Astronomy for continuous feedback throughout the development of this research. J. W. acknowledges the support by the National Science Foundation under grant No. 2143400.

This publication makes use of data products from the Wide-field Infrared Survey Explorer, which is a joint project of the University of California, Los Angeles, and the Jet Propulsion Laboratory/California Institute of Technology, funded by the National Aeronautics and Space Administration.

The views expressed in this article are those of the author and do not necessarily reflect the official policy or position of the Air Force, the Department of Defense, or the U.S. Government.

Software: Astropy (Astropy Collaboration et al. 2013, 2018), Dynesty (Speagle 2020), Matplotlib (Hunter 2007), Pandas (McKinney et al. 2010), Scipy (Virtanen et al. 2020).

ORCID iDs

Michael K. Plummer https://orcid.org/0000-0002-4831-0329
Ji Wang (王吉) https://orcid.org/0000-0002-4361-8885

References

Ackerman, A. S., & Marley, M. S. 2001, ApJ, 556, 872
Agol, E., Dorn, C., Grimm, S. L., et al. 2021, PSJ, 2, 1
Albrecht, E. M., Jensen, A. M., Jensen, E. G., et al. 2022, JAnSc, 69, 120
Allard, F., & Hauschildt, P. H. 1995, ApJ, 445, 433
Allard, F., Hauschildt, P. H., Alexander, D. R., Tamanai, A., & Schweitzer, A. 2001, ApJ, 556, 357
Allard, F., Homeier, D., & Freytag, B. 2012, RSPTA, 370, 2765
Allers, K. N., & Liu, M. C. 2013, ApJ, 772, 79
Apai, D., Karalidi, T., Marley, M. S., et al. 2017, Sci, 357, 683
Apai, D., Nardiello, D., & Bedin, L. R. 2021, ApJ, 906, 64
Apai, D., Radigan, J., Buenzli, E., et al. 2013, ApJ, 768, 121
Artigau, É., Bouchard, S., Doyon, R., & Lafrenière, D. 2009, ApJ, 701, 1534
Artigau, É., Doyon, R., Lafrenière, D., et al. 2006, ApJL, 651, L57
Astropy Collaboration, Price-Whelan, A. M., Sipőcz, B. M., et al. 2018, AJ, 156, 123

Astropy Collaboration, Robitaille, T. P., Tollerud, E. J., et al. 2013, A&A, 558, A33
Barman, T. S., Konopacky, Q. M., Macintosh, B., & Marois, C. 2015, ApJ, 804, 61
Barman, T. S., Macintosh, B., Konopacky, Q. M., & Marois, C. 2011, ApJ, 733, 65
Barnes, J. R., Jeffers, S. V., Haswell, C. A., et al. 2017, MNRAS, 471, 811
Barnes, J. R., Jeffers, S. V., Jones, H. R. A., et al. 2015, ApJ, 812, 42
Baron, E., Hauschildt, P. H., Branch, D., Kirshner, R. P., & Filippenko, A. V. 1996, MNRAS, 279, 799
Bell, C. P. M., Mamajek, E. E., & Naylor, T. 2015, MNRAS, 454, 593
Biller, B. A., Vos, J., Bonavita, M., et al. 2015, ApJL, 813, L23
Biller, B. A., Vos, J., Buenzli, E., et al. 2018, AJ, 155, 95
Bonnefoy, M., Boccaletti, A., Lagrange, A. M., et al. 2013, A&A, 555, A107
Bonnefoy, M., Marleau, G. D., Galicher, R., et al. 2014, A&A, 567, L9
Bonnefoy, M., Zurlo, A., Baudino, J. L., et al. 2016, A&A, 587, A58
Bowler, B. P., Liu, M. C., Dupuy, T. J., & Cushing, M. C. 2010, ApJ, 723, 850
Bowler, B. P., Zhou, Y., Morley, C. V., et al. 2020, ApJL, 893, L30
Brady, M., Bean, J., Seifahrt, A., et al. 2023, AJ, 165, 129
Brandl, B., Bettonvil, F., van Boekel, R., et al. 2021, Msngr, 182, 22
Bryan, M. L., Benneke, B., Knutson, H. A., Batygin, K., & Bowler, B. P. 2018, NatAs, 2, 138
Bryan, M. L., Ginzburg, S., Chiang, E., et al. 2020, ApJ, 905, 37
Buenzli, E., Apai, D., Radigan, J., Reid, I. N., & Flateau, D. 2014, ApJ, 782, 77
Buenzli, E., Marley, M. S., Apai, D., et al. 2015a, ApJ, 812, 163
Buenzli, E., Saumon, D., Marley, M. S., et al. 2015b, ApJ, 798, 127
Burgasser, A. J., & Mamajek, E. E. 2017, ApJ, 845, 110
Chilcote, J., Pueyo, L., De Rosa, R. J., et al. 2017, AJ, 153, 182
Costa, E., Méndez, R. A., Jao, W. C., et al. 2006, AJ, 132, 1234
Croll, B., Muirhead, P. S., Lichtman, J., et al. 2016, arXiv:1609.03587
Crossfield, I. J. M., Biller, B., Schlieder, J. E., et al. 2014, Natur, 505, 654
Currie, T., Burrows, A., Girard, J. H., et al. 2014, ApJ, 795, 133
Currie, T., Burrows, A., Madhusudhan, N., et al. 2013, ApJ, 776, 15
Cutri, R. M., Wright, E. L., Conrow, T., et al. 2014, yCat, 2328, 0
Cutri, R. M., Skrutskie, M. F., van Dyk, S., et al. 2003, yCat, 2246, 0
Donatelli, M., & Reichel, L. 2014, JCoAM, 272, 334
Donati, J. F., Semel, M., Carter, B. D., Rees, D. E., & Collier Cameron, A. 1997, MNRAS, 291, 658
Doyon, R., Lafrenière, D., Artigau, E., Malo, L., & Marois, C. 2010, in Proc. of the Conf. In the Spirit of Lyot 2010: Direct Detection of Exoplanets and Circumstellar Disks, ed. A. Boccaletti, E42
Dulaimi, S., Golden, A., Boyle, R. P., & Butler, R. F. 2023, MNRAS, 518, 4428
Dupuy, T. J., Brandt, T. D., Kratter, K. M., & Bowler, B. P. 2019, ApJL, 871, L4
Dupuy, T. J., Liu, M. C., Evans, E. L., et al. 2023, MNRAS, 519, 1688
Dupuy, T. J., Liu, M. C., Magnier, E. A., et al. 2020, RNAAS, 4, 54
Eriksson, S. C., Janson, M., & Calissendorff, P. 2019, A&A, 629, A145
Fanson, J., Bernstein, R., Angeli, G., et al. 2020, Proc. SPIE, 11445, 114451F
Fitzgerald, M., Bailey, V., Baranec, C., et al. 2019, BAAS, 51, 251
Froning, C., Osterman, S., & Beasley, M. 2006, Proc. SPIE, 6269, 62691V
Gagné, J., Faherty, J. K., Burgasser, A. J., et al. 2017, ApJL, 841, L1
Gaia Collaboration, Brown, A. G. A., Vallenari, A., et al. 2021, A&A, 650, C3
Gauza, B., Béjar, V. J. S., Pérez-Garrido, A., et al. 2015, ApJ, 804, 96
Gillon, M., Jehin, E., Lederer, S. M., et al. 2016, Natur, 533, 221
Gillon, M., Triaud, A. H. M. J., Demory, B.-O., et al. 2017, Natur, 542, 456
Gizis, J. E., Dettman, K. G., Burgasser, A. J., et al. 2015, ApJ, 813, 104
Gonzales, E. C., Faherty, J. K., Gagné, J., et al. 2019, ApJ, 886, 131
Goździewski, K., & Migaszewski, C. 2020, ApJL, 902, L40
GRAVITY Collaboration, Lacour, S., Nowak, M., et al. 2019, A&A, 623, L11
GRAVITY Collaboration, Nowak, M., Lacour, S., et al. 2020, A&A, 633, A110
Gray, R. O., Corbally, C. J., Garrison, R. F., et al. 2006, AJ, 132, 161
Greenbaum, A. Z., Pueyo, L., Ruffio, J.-B., et al. 2018, AJ, 155, 226
Günther, M. N., Zhan, Z., Seager, S., et al. 2020, AJ, 159, 60
Hauschildt, P. H. 1992, JQSRT, 47, 433
Hauschildt, P. H. 1993, JQSRT, 50, 301
Hauschildt, P. H., & Baron, E. 1995, JQSRT, 54, 987
Hauschildt, P. H., Baron, E., & Allard, F. 1997, ApJ, 483, 390
Hauschildt, P. H., Baron, E., Starrfield, S., & Allard, F. 1996, ApJ, 462, 386
Hauschildt, P. H., Starrfield, S., Shore, S. N., Allard, F., & Baron, E. 1995, ApJ, 447, 829
Hébrard, É. M., Donati, J. F., Delfosse, X., et al. 2016, MNRAS, 461, 1465
Heinze, A. N., Metchev, S., Apai, D., et al. 2013, ApJ, 767, 173
Helling, C., Ackerman, A., Allard, F., et al. 2008, MNRAS, 391, 1854
Higson, E., Handley, W., Hobson, M., & Lasenby, A. 2019, S&C, 29, 891
Hinz, P. M., Rodigas, T. J., Kenworthy, M. A., et al. 2010, ApJ, 716, 417
Hoch, K. K. W., Konopacky, Q. M., Barman, T. S., et al. 2022, AJ, 164, 155
Hunter, J. D. 2007, CSE, 9, 90
Ilin, E., Poppenhaeger, K., Schmidt, S. J., et al. 2021, MNRAS, 507, 1723
Jaffe, D. T., Barnes, S., Brooks, C., et al. 2016, Proc. SPIE, 9908, 990821
Janson, M., Bergfors, C., Goto, M., Brandner, W., & Lafrenière, D. 2010, ApJL, 710, L35
Johns, M. 2006, Proc. SPIE, 6267, 626729
Jones, A., Noll, S., Kausch, W., Szyszka, C., & Kimeswenger, S. 2013, A&A, 560, A91
Jones, H. R. A., & Tsuji, T. 1997, ApJL, 480, L39
Karalidi, T., Apai, D., Marley, M. S., & Buenzli, E. 2016, ApJ, 825, 90
Kasting, J. F., Whitmire, D. P., & Reynolds, R. T. 1993, Icar, 101, 108
Kervella, P., Arenou, F., Mignard, F., & Thévenin, F. 2019, A&A, 623, A72
Khokhlova, V. L. 1985, ASPRv, 4, 99
Khokhlova, V. L., Rice, J. B., & Wehlau, W. H. 1986, ApJ, 307, 768
Kochukhov, O. 2016, in Cartography of the Sun and the Stars, Lecture Notes in Physics, Vol. 914, ed. J.-P. Rozelot & C. Neiner (Cham: Springer Verlag), 177
Kochukhov, O., Makaganiuk, V., & Piskunov, N. 2010, A&A, 524, A5
Kopparapu, R. K., Ramirez, R., Kasting, J. F., et al. 2013, ApJ, 765, 131
Lagrange, A. M., Bonnefoy, M., Chauvin, G., et al. 2010, Sci, 329, 57
Lagrange, A. M., De Bondt, K., Meunier, N., et al. 2012, A&A, 542, A18
Lagrange, A. M., Gratadour, D., Chauvin, G., et al. 2009, A&A, 493, L21
Lagrange, A. M., Rubini, P., Nowak, M., et al. 2020, A&A, 642, A18
Lane, C., Hallinan, G., Zavala, R. T., et al. 2007, ApJL, 668, L163
Lavie, B., Mendonça, J. M., Mordasini, C., et al. 2017, AJ, 154, 91
Lawrence, A., Warren, S. J., Almaini, O., et al. 2012, yCat, 2314, 0
Liu, M. C., Dupuy, T. J., & Allers, K. N. 2016, ApJ, 833, 96
Lord, S. D. 1992, A New Software Tool for Computing Earth's AtmosphericTransmission of Near- and Far-infrared Radiation NASA Technical Memorandum 103957
Luger, R., Bedell, M., Foreman-Mackey, D., et al. 2021, arXiv:2110.06271
Luger, R., Sestovic, M., Kruse, E., et al. 2017, NatAs, 1, 0129
Macintosh, B., Graham, J. R., Barman, T., et al. 2015, Sci, 350, 64
Madhusudhan, N., Burrows, A., & Currie, T. 2011, ApJ, 737, 34
Maihara, T., Iwamuro, F., Yamashita, T., et al. 1993, PASP, 105, 940
Marconi, A., Abreu, M., Adibekyan, V., et al. 2022, Proc. SPIE, 12184, 1218424
Marley, M. S., Saumon, D., Cushing, M., et al. 2012, ApJ, 754, 135
Marley, M. S., Saumon, D., & Goldblatt, C. 2010, ApJL, 723, L117
Marley, M. S., Seager, S., Saumon, D., et al. 2002, ApJ, 568, 335
Marois, C., Macintosh, B., Barman, T., et al. 2008, Sci, 322, 1348
Marois, C., Zuckerman, B., Konopacky, Q. M., Macintosh, B., & Barman, T. 2010, Natur, 468, 1080
Martin, D. V., Sethi, R., Armitage, T., et al. 2023, arXiv:2301.10858
Mawet, D., Fitzgerald, M., Konopacky, Q., et al. 2019, BAAS, 51, 134
McCarthy, P. J., Fanson, J., Bernstein, R., et al. 2016, Proc. SPIE, 9906, 990612
McKinney, W., et al. 2010, in Proc. the 9th Python in Science Conf., 56
Miles, B. E., Biller, B. A., Patapis, P., et al. 2023, ApJL, 946, L6
Millar-Blanchaer, M. A., Girard, J. H., Karalidi, T., et al. 2020, ApJ, 894, 42
Mollière, P., Stolker, T., Lacour, S., et al. 2020, A&A, 640, A131
Morley, C. V., Marley, M. S., Fortney, J. J., et al. 2014, ApJ, 787, 78
Morris, B. M., Agol, E., Davenport, J. R. A., & Hawley, S. L. 2018, ApJ, 857, 39
Morzinski, K. M., Males, J. R., Skemer, A. J., et al. 2015, ApJ, 815, 108
Mulders, G. D., Pascucci, I., & Apai, D. 2015, ApJ, 798, 112
National Academies of Sciences, Engineering, & Medicine 2021, Pathways to Discovery in Astronomy and Astrophysics for the 2020s (Washington, DC: The National Academies Press)
Noll, K. S., Geballe, T. R., Leggett, S. K., & Marley, M. S. 2000, ApJL, 541, L75
Noll, S., Kausch, W., Barden, M., et al. 2012, EGU General Assembly Conf., 14, 9813
O'Malley-James, J. T., & Kaltenegger, L. 2017, MNRAS, 469, L26
Oppenheimer, B. R., Kulkarni, S. R., Matthews, K., & Nakajima, T. 1995, Sci, 270, 1478
Packham, C., Honda, M., Okamoto, Y. K., et al. 2014, in TMT in the Astronomical Landscape of the 2020s, Thirty Meter Telescope Science Forum, ed. M. Dickinson & H. Inami, 20
Pai Asnodkar, A., Wang, J., Gaudi, B. S., et al. 2022, AJ, 163, 40
Paudel, R. R., Gizis, J. E., Mullan, D. J., et al. 2018, ApJ, 858, 55
Paudel, R. R., Gizis, J. E., Mullan, D. J., et al. 2020, MNRAS, 494, 5751
Petit, P., Dintrans, B., Solanki, S. K., et al. 2008, MNRAS, 388, 80
Petrus, S., Chauvin, G., Bonnefoy, M., et al. 2023, A&A, 670, L9

Piskunov, N. E., Tuominen, I., & Vilhu, O. 1990, A&A, 230, 363
Plummer, M. K., & Wang, J. 2022, ApJ, 933, 163
Radigan, J. 2014, ApJ, 797, 120
Radigan, J., Jayawardhana, R., Lafrenière, D., et al. 2012, ApJ, 750, 105
Radigan, J., Lafrenière, D., Jayawardhana, R., & Artigau, E. 2014, ApJ, 793, 75
Reiners, A., & Basri, G. 2008, ApJ, 684, 1390
Reiners, A., & Basri, G. 2010, ApJ, 710, 924
Roettenbacher, R. M., & Kane, S. R. 2017, ApJ, 851, 77
Ruffio, J.-B., Konopacky, Q. M., Barman, T., et al. 2021, AJ, 162, 290
Sabotta, S., Schlecker, M., Chaturvedi, P., et al. 2021, A&A, 653, A114
Saumon, D., & Marley, M. S. 2008, ApJ, 689, 1327
Scalo, J., Kaltenegger, L., Segura, A. G., et al. 2007, AsBio, 7, 85
Schweitzer, A., Hauschildt, P. H., Allard, F., & Basri, G. 1996, MNRAS, 283, 821
Showman, A. P., Tan, X., & Zhang, X. 2019, ApJ, 883, 4
Shuster, M. D. 1993, ITAES, 29, 263
Skemer, A. J., Hinz, P. M., Esposito, S., et al. 2012, ApJ, 753, 14
Skemer, A. J., Marley, M. S., Hinz, P. M., et al. 2014, ApJ, 792, 17
Skidmore, W. & TMT International Science Development Teams & Science Advisory Committee T. 2015, RAA, 15, 1945
Skilling, J. 2004, in AIP Conf. Ser. 735, Bayesian Inference and Maximum Entropy Methods in Science and Engineering: 24th Int. Workshop on Bayesian Inference and Maximum Entropy Methods in Science and Engineering, ed. R. Fischer, R. Preuss, & U. V. Toussaint (Melville, NY: AIP), 395
Skilling, J. 2006, BayAn, 1, 833
Snellen, I. A. G., Brandl, B. R., de Kok, R. J., et al. 2014, Natur, 509, 63
Snellen, I. A. G., & Brown, A. G. A. 2018, NatAs, 2, 883
Speagle, J. S. 2020, MNRAS, 493, 3132
Su, K. Y. L., Rieke, G. H., Stapelfeldt, K. R., et al. 2009, ApJ, 705, 314
Szentgyorgyi, A., Baldwin, D., Barnes, S., et al. 2018, Proc. SPIE, 10702, 107021R
Thomas-Osip, J. E., Prieto, G., Johns, M., & Phillips, M. M. 2008, Proc. SPIE, 7012, 70121U
Tsuji, T., Ohnaka, K., & Aoki, W. 1996a, A&A, 305, L1
Tsuji, T., Ohnaka, K., Aoki, W., & Nakajima, T. 1996b, A&A, 308, L29
Tuomi, M., Jones, H. R. A., Butler, R. P., et al. 2019, arXiv:1906.04644
van Leeuwen, F. 2007, A&A, 474, 653
Vandal, T., Rameau, J., & Doyon, R. 2020, AJ, 160, 243
Vida, K., Kővári, Z., Pál, A., Oláh, K., & Kriskovics, L. 2017, ApJ, 841, 124
Virtanen, P., Gommers, R., Oliphant, T. E., et al. 2020, NatMe, 17, 261
Vogt, S. S., Penrod, G. D., & Hatzes, A. P. 1987, ApJ, 321, 496
Vos, J. M., Allers, K. N., & Biller, B. A. 2017, ApJ, 842, 78
Vos, J. M., Burningham, B., Faherty, J. K., et al. 2023, ApJ, 944, 138
Wang, J., David, T. J., Hillenbrand, L. A., et al. 2018a, ApJ, 865, 141
Wang, J., Kolecki, J. R., Ruffio, J.-B., et al. 2022a, AJ, 163, 189
Wang, J., Prato, L., & Mawet, D. 2017, ApJ, 838, 35
Wang, J., Wang, J. J., Ma, B., et al. 2020, AJ, 160, 150
Wang, J. J., Gao, P., Chilcote, J., et al. 2022b, AJ, 164, 143
Wang, J. J., Graham, J. R., Dawson, R., et al. 2018b, AJ, 156, 192
Wang, J. J., Ruffio, J.-B., Morris, E., et al. 2021, AJ, 162, 148
Wheatley, P. J., Louden, T., Bourrier, V., Ehrenreich, D., & Gillon, M. 2017, MNRAS, 465, L74
Wilson, D. J., Froning, C. S., Duvvuri, G. M., et al. 2021, ApJ, 911, 18
Witte, S., Helling, C., Barman, T., Heidrich, N., & Hauschildt, P. H. 2011, A&A, 529, A44
Wright, E. L., Eisenhardt, P. R. M., Mainzer, A. K., et al. 2010, AJ, 140, 1868
Yang, H., Apai, D., Marley, M. S., et al. 2016, ApJ, 826, 8
Zendejas, J., Segura, A., & Raga, A. C. 2010, Icar, 210, 539
Zhang, X. 2020, RAA, 20, 099
Zhang, X., & Showman, A. P. 2014, ApJL, 788, L6
Zhou, Y., Apai, D., Bedin, L. R., et al. 2020a, AJ, 159, 140
Zhou, Y., Apai, D., Schneider, G. H., Marley, M. S., & Showman, A. P. 2016, ApJ, 818, 176
Zhou, Y., Bowler, B. P., Apai, D., et al. 2022, AJ, 164, 239
Zhou, Y., Bowler, B. P., Morley, C. V., et al. 2020b, AJ, 160, 77
Zink, J. K., Hardegree-Ullman, K. K., Christiansen, J. L., et al. 2020, AJ, 160, 94
Zuckerman, B., Bessell, M. S., Song, I., & Kim, S. 2006, ApJL, 649, L115
Zuckerman, B., Rhee, J. H., Song, I., & Bessell, M. S. 2011, ApJ, 732, 61
Zurlo, A., Vigan, A., Galicher, R., et al. 2016, A&A, 587, A57